ACCELERATOR R & D

CURRENT STATUS AND PLANS FOR THE NSCL CONTROL SYSTEM SOFTWARE

Lynn Foth and John Priller

During the past year we have improved upon the existing control system applications at NSCL, eliminating several known problems and increasing responsiveness and usability.

KIM, the primary cyclotron control program (see NSCL Annual Report 1988, pg. 133), underwent extensive modification to reduce delays between device adjustments and results appearing to the operator. Several of the control system's support modules, the Control Panel I/O and ArcNet Communications modules in particular, were also modified with that goal in mind. Further modifications to these modules (and the other modules in the control system) were made necessary by a major version upgrade in the workstations' operating system software (VAX VMS).

Work on extending and expanding the control system is proceeding. The ArcNet Multitasker has been re-christened the ArcNet Server (to better reflect its true function), and is approaching its final debugging stage. It should be installed and available to application programs in the Spring of 1990. When in place, it will allow several control programs to simultaneously access the ArcNet communications card within the control system workstations, rather than one program at a time, as is currently the case.

Still on the agenda for future control system developments are the General Device Layer, the Pseudo-Device Layer, and the CAMAC, Modicon, and Bit I/O communications modules. These are described in the 1988 NSCL Annual Report, under "Main Console and Software", and, when available, will greatly expand the power and scope of control system applications.

Work on the equipment interface level (see NSCL Annual Report 1988, page 127) is currently proceeding on two fronts - further installation of controls and a general software upgrade.

As beamlines in the Transfer Hall and A1200 Analysis Hall are built, controls interfaces are being installed. One new VME station has been added to handle the Transfer Hall. The A1200 Analysis Hall will be picked up on the station which previously handled the interim beamline segment from the K1200 Cyclotron to the 4 pi and 92" scattering chamber. This control installation work is going smoothly due to the use of known, lab-standard interfacing techniques.

The general upgrade is one of the last VME software tasks currently scheduled. There are multiple goals for this upgrade:

1) integrate new features developed at Fermilab;
2) migrate to a system based on the pSOS kernel;
3) allow for use of the Motorola 68020/68881 chip set in selected stations;
4) bring all stations up to the same level of code and function;
5) delete obsolete features and consolidate others.

This upgrade must be completed before the K1200 is scheduled to run again. In addition to the above upgrade goals, there is the possibility that some of the VME and Vax Network Level support which Fermilab has added for their D0 project will aid us in building the General Device Layer of the Main Console (NSCL Annual Report 1988, page 132).

CURRENT STATUS OF THE NSCL PHASE II BEAMLINE ELECTRONICS FABRICATION AND INSTALLATION

A. McGilvra

The electronics for the Phase II beamline (beamline that connects the K-1200 cyclotron to all the experimental vaults) are in various stages of completion. The Phase II electronics (see NSCL Phase II Beamline Electronics from the 1988 Annual Report for a complete description) consists of controls, power supplies, and instrumentation. These are distributed between two major installations: the analysis hall beamline (A1200) which is a single S-shaped beamline at the exit of the K-1200 cyclotron, and the transfer hall which is a multiple beamline switchyard that connects the K-500 cyclotron and the K-1200 cyclotron (via the A1200) to five experimental vaults. Each of these halls has an associated group of control racks that contain the electronics. The control racks for the transfer hall also contains many of the electronics for the five experimental vaults.

Controls

VME crates and modules: Used for analog settings and readings and for serial communications with devices that are controlled via a serial line instead of by analog signals.
Transfer hall status: All purchased and installed.
Analysis hall status: All purchased, none installed.

Gould-Modicon PLC (programmable logic controller) modules: Used for interlock logic control; turn devices on and off, tell status of water flow switches, etc.
Transfer hall status: All purchased and installed.
Analysis hall status: All purchased, none installed.

Power Supplies

20 Volt, 20 Amp DC power supplies: Used to power the quadrupole focusing magnets. Quantity needed is 49.
Transfer hall status: All built, tested, and installed.
Analysis hall status: All built, one tested, none installed.

10 Volt, 100 Amp DC power supplies: Used to power the dipole steering magnets. Quantity needed is nine.
Transfer hall status: One built and tested, five in production.
Analysis hall status: Four in production.

Instruments

Beam current meters: Used to read the beam current at several points on the beamline. Quantity needed is 12.
Transfer hall status: All built, one tested, none installed.
Analysis hall status: All built, none tested, none installed.

Bang-bang servos: Used to control motor drives for moving beam diagnostic apparatus and experimental apparatus. Quantity needed is 21.
Transfer hall status: All built, three tested, three installed.
Analysis hall status: All built, none tested, none installed.

Cryogenic monitor unit: Used to monitor health signals of the magnet cryostats; monitors helium pressure, helium level, and magnet lead voltage drop. Quantity needed is 33.

Transfer hall status: All built, all tested, all installed.
Analysis hall status: All built, all tested, none installed.

Dual channel thermocouple vacuum gauge controller: Used to read vacuum from two thermocouple vacuum sensors. Quantity needed is 19.
Transfer hall status: All built, seven tested, none installed.
Analysis hall status: All built, none tested, none installed.

Local monitoring devices: Used to monitor information at the control racks. There are three of these: the LED panel is used to monitor six status functions on 24 cryostats, two are needed; the cryogenic dual meter selector panel is used to read helium level and helium pressure from 24 cryostats, two are needed; and the vacuum dual meter selector panel used to read vacuum information, eight are needed.
Transfer hall status: All built, all tested, one of each installed.
Analysis hall status: All built, all tested, none installed.

CURRENT STATUS OF THE K1200 RF

J. Vincent, J. Brandon, F. Pigeaud, J. Ottarson

1. Introduction

Last year's Annual Report described the initial operation of the K1200 rf system and discussed the associated problems. The difficulties being actively addressed at that time involved the rf amplifiers, Aydin power supply, corona rings, dee stem insulators, and minor electronic problems. Fortunately, their are no new problems to report, and each of the difficulties described last year has either been corrected, or will be so before the next running period begins.

Another change that will reduce the strain on the rf system is the new central region which reduces the required rf voltage by about 20%. These new parts should also be installed before the next running period.

This paper will give a brief overview of solutions to the known problems and direct the reader to detailed technical papers for more information.

2. RF Amplifiers

Last year's annual report described the multiple failures we were experiencing with the RCA 4648 tetrode. The problem with these tubes appears to be due to changes in the materials and/or the conditioning process used at the factory. The factory denies that these changes are responsible for our problems, but our statistical evidence indicates otherwise.

The two tubes we have, which went through the extended processing treatment at the factory, have run in all of our amplifiers for the longest periods to date without a problem. FNAL and LAMPF have apparently also had difficulties with related tubes. The specific problem seems to be associated with the vacuum in the tubes deteriorating after the rf is initially applied. The vacuum then remains poor, leading to failures of one sort or another depending on tube type. Regardless of the exact cause, statistical evidence here and elsewhere indicates that these tubes are not what they used to be. For these reasons, we have elected to retrofit all of our amplifiers with a more robust and less costly tube as described in last year's annual report. RF note #107 describes the selection of the new tube in detail.

As indicated above, we are currently changing all of our amplifiers to use the TH555 model from Thomson. The development of this amplifier is complete, and has been tested into a dummy load, open circuit, and cyclotron resonator up to full power across our entire operating band. The newly designed amplifier seems to be very robust and stable. We have no reason to anticipate problems with reliability, since the prototype has run for about 3000 hours without a problem. NSCL RF note #108 describes and analyzes the new amplifiers in some detail. Four tubes and three sockets are currently in house, and all the parts necessary to convert our current amplifiers are being procured. We will have all the amplifiers converted and ready for operation in July 1990.

3. Aydin Power Supply

The rectifier choke problems described in last year's annual report appear to be solved. The Aydin supply has been used as the primary bias supply for the final amplifiers for most of this year. The only problems which remain are associated with its controls, internal relay logic, and high voltage distribution portions. All of these aspects are enclosed in a single cabinet whose design was not optimum. We have

designed and are procuring two new cabinets and associated parts to resolve these remaining issues. However, these problems have not prevented use of the supply. This final upgrade will be done before the next running period or shortly thereafter.

4. Corona Rings and Dee Stem Insulators

A great deal was said in last year's annual report about the dee stem insulators and corona rings. Two problems were being addressed.

1. Vacuum leaks developing over time.
2. Insulator failures, which may or may not be related to item 1.

We proceeded along three paths to find a solution to this problem.

1. Investigate the ceramic properties, with the aim of finding a treatment or material which is more robust.
2. Try sealing the ceramic to resonator joints with O-rings rather than indium.
3. Increase the air flow in these locations.

With regard to item one, results of our studies are not fully analyzed. We found two methods of treatment which increased the electrical capabilities and robustness of these materials. One method involves coating the surface with a layer of TiN about 100 angstroms thick to reduce secondary electron emission and the other involves "graying" the insulator at a temperature of about 1450 degrees Celsius with a 75% dry Nitrogen and 25% dry Hydrogen atmosphere.

Both of the above methods seem to reduce the secondary electron emission coefficient to levels of 2 or 3 from around 9. However, single surface or two surface multipactoring effects still may occur at these levels. The most interesting finding was the effect of the treatments with respect to electromagnetic radiation in the ultraviolet to gamma frequency range. Untreated material seemed to require many hours to recover from such an exposure whereas treated material was virtually unaffected by the exposure. We have not finished studying this effect, nor do we fully understand it. No report has been completed as yet, though it seems we are close to resolving the dominant problem. We are in the process of finding equipment and vendors who can perform these treatments on the cyclotron insulators. This will allow us to make actual tests on the materials in the machine. These treatments would be appeared to both the dee stem insulators and the coupler insulators.

With regards to item 2, we have tested O-rings made of silicone rubber on the C system upper stem. We ran the dees near full voltage at various frequencies and as yet have found no adverse effect due to the O-rings. The preferred material for these O-rings would be pure Butyl rubber rather than silicone rubber, but Butyl rubber O-rings are not generally "on the shelf" items. Silicone rubber is almost as good as Butyl rubber with respect to rf losses but it has a much greater Helium permeability. We will install the Butyl rubber O-rings when they become available, then repeat the tests.

If the long term result of using O-rings is favorable, then possibly a year from now we will begin converting all of the stem seals to O-rings. Along with this change we may be able to gray the dee stem insulators to increase their electrical robustness. It will be necessary to have the insulators shortened a little to allow for the O-ring sealing mechanism.

With respect to item 3, we increased the air flow on the B station upper and lower stems. Whether this change has caused any improvement or not cannot be determined until summer when the building is hotter and the relative humidity in the equipment areas increases significantly.

In the past sparking problems in these areas were much more noticeable during the summer.

5. RF Electronics

The RF electronics have not required any modification, seem to work well and are reliable. The only change made this year involved replacing the phase meter that reports the dee to dee phase to the control system. We installed two Hewlett Packard Vector Voltmeters and connected them to the general control system. We know of no other problems associated with the electronics. We may wish to make improvements or enhancements in the future, but none are currently planned or envisioned.

6. Operating Experience

The beginning of the year was marred by tube failures and Aydin power supply failures that were not completely understood. However, the last part of the year the RF system was running reliably.

7. Conclusion

All the RF system problems appear to have been resolved. The reliability of the system is expected to be very high when the next running period begins next August. Other than some further testing and development on the cyclotron resonators with respect to insulators, no other major changes or enhancements are currently envisioned. However, it is assumed that in the next running period we will begin to run higher energy beams for prolonged periods of time. This may require further alterations to increase the reliability of stressed components.

ACCELERATION OF MOLECULAR IONS IN THE K1200 SUPERCONDUCTING CYCLOTRON

T.A. Antaya, M.L. Mallory, F. Marti, P.S. Miller, J.A. Nolen, D. Poe, B.M. Sherrill and A.F. Zeller

The NSCL K1200 superconducting cyclotron was designed to accelerate heavy ions in the energy per nucleon range from 18 to 200 MeV in first harmonic mode. The operating diagram does not include protons at any energy, deuterons below E/A=140 MeV, ^{3}He below E/A=60 MeV, nor alphas below E/A=30 MeV, unless these nuclei are accelerated as components of molecular ions. Examples of potentially useful ions are: H_2^+, D_2^+, $(H\text{-}D)^+$, $(H\text{-}He)^+$, and $(D\text{-}He)^+$. Molecular ions of these species have been extracted from the NSCL CPECR ion source at the 5 microamp or more intensity level, and the last three have also been accelerated and extracted recently from the cyclotron at E/A= 70, 30 MeV and 20 MeV, respectively.

These beams are useful to calibrate light ion detectors used in heavy ion experiments and also for independent light ion research. The $(H\text{-}He)^+$ ion at 30 MeV/A was used to calibrate both particle and gamma counters for an experiment using the Washington University Dwarf Ball and the Oak Ridge BaF_2 detectors in coincidence. The reaction used was ^{12}C(p,p'gamma), observing the 15.1 MeV gamma ray in coincidence with the inelastically scattered protons. The $(H\text{-}D)^+$ ion at 70 MeV/A was used to simultaneously provide 70 MeV protons and 140 MeV deuterons to calibrate the phoswich light ion detectors of the MSU 4Pi detector and its forward array. The two components of the mixed molecules have different magnetic rigidities after stripping so that a pure beam of either species can be sent to the scattering target if this is desireable for the experiment or calibration run.

There is an emittance increase due to the Coulomb repulsion when the molecules are dissociated by the target or a stripper foil in the beamline, but the increase is estimated to be small except for the lowest velocity ions. To see if the 200 MeV H_2^+ ion can be used to obtain high quality 200 MeV protons the effects of the Coulomb explosion have been estimated. The interatomic spacing of this molecular ion is 1.06 angstrom, giving a kinetic energy of 7 eV per proton from the Coulomb repulsion following stripping. Velocity additions in the transverse and longitudinal directions predict a growth of 0.2 mr and 4 parts in 10^4 energy spread, respectively. These numbers are smaller than the intrinsic beam properties before stripping. At low velocities, however, the effects of the Coulomb explosion can dominate the emittance.

The molecular ions have low dissociation energies, 2.7 eV for the diatomic hydrogen ions and 1.9 eV for the diatomic hydrogen-helium ions. These low binding energies make these ions susceptible to loss by vacuum attenuation and electromagnetic stripping. Models for estimating the vacuum attenuation effect and comparing the magnitude of electromagnetic stripping with that observed in other accelerators, such as TRIUMF (H^- ions), indicate that most of these molecular beams can be accelerated even in superconducting cyclotrons with 5T magnetic fields such as the ones at NSCL. For example, Fig. 1 shows predicted vacuum attenuation curves for 20 MeV/A ^{4}He-D ions accelerated in the K1200 cyclotron using the same model normally used for heavy ion electron loss attenuation. The attenuation observed for this beam was less than a factor of two over the range from 20 to 40" radius (the range of the radial probe). This is consistent with the vacuum in the beam chamber being in the high 10^{-7} torr range.

In the table we list properties of several

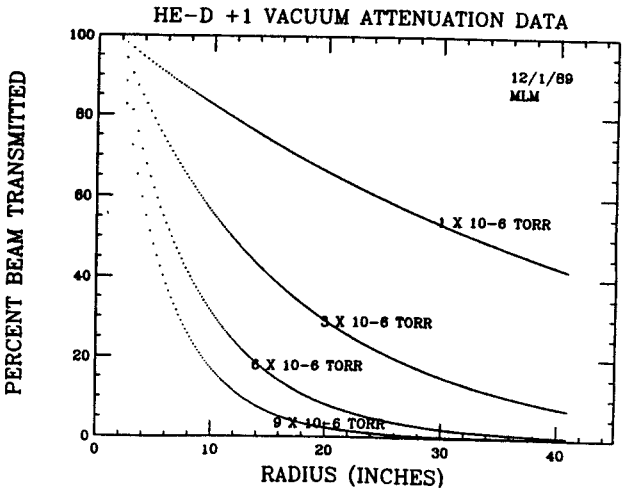

Fig. 1. Predicted vacuum attenuation curves for 20 MeV/A ^{4}He-D ions in the K1200 for various vacuum conditions. The observed curve was consistent with the model used to calculate these curves, assuming the pressure was in the upper 10^{-7} torr range.

interesting molecular ions. Some of these are easy to develop, while others are only shown for general interest, e.g. the Xe_2^+ ion which is not of interest for the present cyclotrons, but may be useful for some future accelerator. The molecular ions involving ^{3}He and tritium may be impractical because of the high gas feed rates required to form these beams in the CPECR. Such isotopes may require the development of a special more efficient source geometry. The diatomic molecular ions shown in the table have dissociation engergies ranging from 0.85 to 4.8 eV, compared to 0.75 eV for H^-.

The H_2^+ ions in the 100-200 Mev/A energy range may begin to show some electromagnetic stripping. The rate of stripping is related to the parameter vB/D_e, the velocity times the magnetic field divided by the dissociation energy. At 200 MeV/A in the K1200 this parameter for the diatomic hydrogen ion is about 1.6 times worse than for the H^- ions at 520 MeV in the TRIUMF cyclotron. The path length in the K1200 is about 15 times less, however.

Table: Properties of Several Molecular Ions

Molecule	D(eV)	M	q/A	Analog	K500 N=1(MeV/A)	K1200 MeV/A	Date extracted & E/A
H_2^+	2.65[1,2]	2	.50	D^+	53-80	135-200	
$^3HeH^{++}$	.85[2]	4	.50	D^+	53-80	135-200	
$^4HeH^{++}$	.85[2]	5	.40	Ne^{8+}	33-63	80-160	
HD^+	2.67[2]	3	.333	C^{4+}	22-53	52-128	1/28/90 70MeV/A
$^4He^3He^{++}$	1.3[3]	7	.286	$^{14}N^{4+}$	16-40	38-100	
HT^+	2.67[2]	4	.25	O^{4+}	13-33	40-74	40 based on α's
$^3HeH^+$	1.85[2]	4	.25	O^{4+}	13-33	40-74	40 based on α's
DT^+	2.65[1,2]	5	.20	Ne^{4+}	8-22	19-48	
$^4HeH^+$	1.85[2]	5	.20	Ne^{4+}	8-22	19-48	12/4/89 30MeV/A
$^3HeD^+$	1.85[2]	5	.20	Ne^{4+}	8-22	19-48	
$^4HeD^+$	1.85[2]	6	.167	C^{2+}	8-15	19-28	12/4/89 20Mev/A
$^3He_2^+$	2.2[1,3]	6	.167	C^{2+}	8-15	19-28	
$^4He^3He^+$	2.2[1,3]	7	.143	N^{2+}	-	19-21	
$^4He_2^+$	2.2[1,3]	8	.125	O^{2+}	-	-	
BeH^+	3.2[1]	10					
CH^+	4.09[1]	13					
OH^+	4.8[1]	17					
NeH^+	2.08[4]	21					
Ne_2^+	1.35[5]	40					
Ar_2^+	1.04[1]	80					
Xe_2^+	.97[1]	248-272					
$^4HeH_2^+$	.27[6]	6	.167	C^{2+}	8-15	19-28	

(For comparison, the dissociation energy of H^- is 0.75 eV[7] .)

Lowest available light ion energies (First harmonic)
Total Energy (MeV)

Ion	K500 Molecular	K500 Atomic	K1200 Molecular	K1200 Atomic	
p	13	-	19	-	
d	8	106	38	280	
^3He	18	66	57	156	
α	32	52	76	112	(lowest run:160(40MeV/A))

References for the Table

1. "AIP Handbook", Third Ed, ed D.E. Gray, 1972.
2. "Molecular Spectra and Molecular Structure", Vol 4, K.P. Huber and G. Herzberg, 1979.
3. A. Belkacem et al, Phys Rev Let 63,2555(1989).
4. V. Bondvlev P.K. Pearson and H.F. Schaefer, J Chem Phys 55, 5804(1971).
5. T.L. Gilbert and A.C. Wahl, J Chem Phys 55, 5247(1971).
6. R.E. Kari and I.G. Csizmadia, J Chem Phys 56, 4337(1972).
7. H. Hotop and W.C. Lineberger, J Phys Chem Ref Data 14, 731(1985).

SUPERCONDUCTING BEAMLINE QUADRUPOLES PROGRESS

J.C. DeKamp, C.T. Magsig, J.A. Nolen, A.F. Zeller

Construction of quadrupole doublets made good progress over the past year[1]. Focussing requirements for the A1200 experimental line[2] have changed the total number of doublet assemblies from 23 to 21 with 2 triplet assemblies being added.

Doublet Construction and Installation

All of the 21 doublets presently budgeted for Phase 2 beamlines are complete. Eight doublets were tested at the CTI 1400 He liquefier test station. Currently (2/90) a total of 13 doublets are installed in the transfer hall, N2, N3, and S1 vault areas as shown in Fig. 1. Cryogenic lines to these magnets are 80% complete and many of the magnets have already been tested in-place. Measured and calculated fields of a representative quadrupole are shown in Fig. 2. A February 1990 view of the transfer hall installation is shown in Fig. 3.

Three of the doublets assembled have had operational problems which required disassembly for repair. Two doublets had He leaks to the insulating vacuum and one had a broken coil. One of the doublets with a He leak has been repaired and reassembled, the other 2 doublets have repairs in progress. One other doublet is also undergoing repair due to the occurrence of a ruptured LHe container.

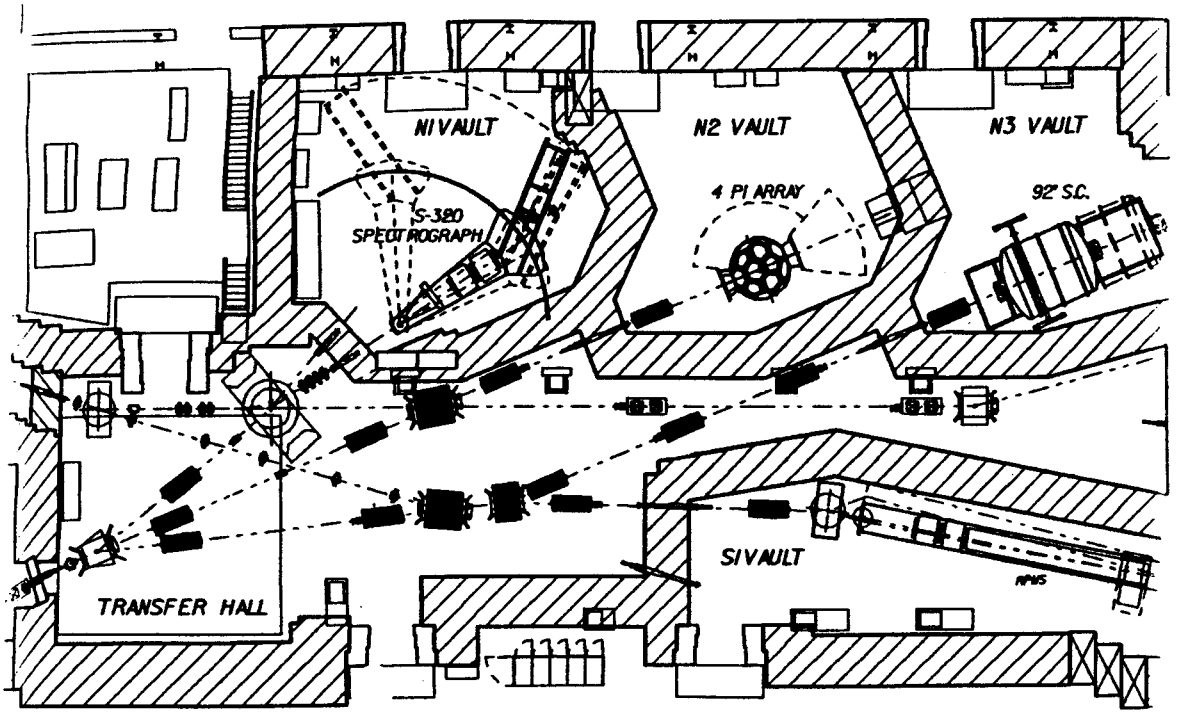

Fig. 1 Phase 2 transfer hall and vault areas. The magnets which are installed are shown in solid black. The 3 large devices are superconducting dipoles.

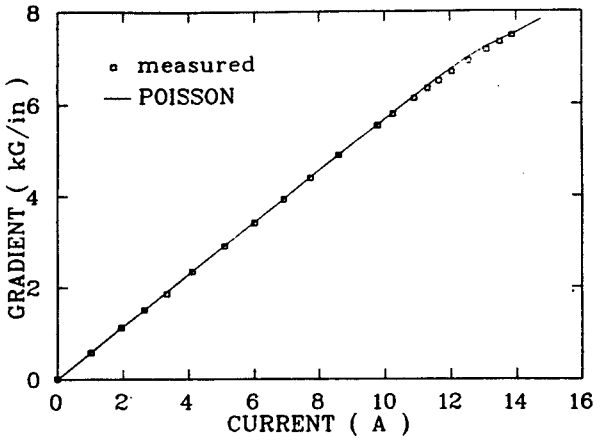

Fig. 2 Measured and calculated gradients for the beamline quad. The POISSON gradients were calculated using the permeability curve furnished by the vendor of the iron assemblies.

Fig. 3 View of present transfer hall installation.

Ruptured LHe Container Incident

During magnet installation in the transfer hall, a very small He system leak to the insulating vacuum was noticed. The leak was not seen until the insulating vacuum was pumped out and the cryostat vacuum welds were being checked. The He system had already been leak checked in the conventional manner. At this time the cryogenic manifold between the magnets was completely welded except for the vacuum jacket before the first doublet on the insulating vacuum. This uncompleted section was temporarily sealed in place to hold cryostat vacuum so final testing could be done. There were a total of 7 magnet cryostats which shared the same vacuum. The leak was then narrowed down to the He gas return manifold line by isolating different parts of the system under He pressure, leaving the remainder of the He system under vacuum. The plan was to narrow down the area of the leak between 2 magnet cryostats and then cut back into the vacuum jacket at the joint between them. This was to be accomplished by pumping out the He gas return line, venting it to atmospheric nitrogen, and then letting He flow into the line from a magnet LHe container in a defined direction while having to diffuse through the nitrogen in the other direction. By using each magnet LHe container, letting the He flow alternatively in opposite directions, and watching the leak indicator response time the leak area could be found. Because of poor sensitivity using warm He, the magnets were cooled down to make cold He available and to improve the cryostat vacuum by cryopumping. Two containers were initially filled with LHe. After filling the He gas return line was pumped out and the cryostat vacuum pumped to reduce the high He background. The high He background also affected the doublet LHe boiloff rates, making them much higher than normal. The boiloff rate and container pressures were watched as only current leads were readily available for return of boiloff gas. The leads are quite restrictive and can handle a limited amount of flow without an increase in container pressure. At the end of normal working hours the insulating vacuum He background was decreasing as was the LHe boiloff rates and container pressures of the 2 doublets. All LHe containers had only a primary relief consisting of a commercial rupture disc assembly. Early the next morning one of the LHe containers ruptured to the insulating vacuum

causing the temporarily sealed section of the vacuum jacket to open and vent the He to atmosphere. The event was noticed by a cyclotron operator on duty at the time. Examination of the doublets which had LHe showed that one had collapsed magnet bore tubes, it's overpressure rupture disc had it's foil membrane broken but the vacuum support for the foil had not opened. Examination of the other doublet showed it's rupture disc to have blown it's safety disc normally; no damage to the cryostat was noticed. Shown in Fig. 4 are both rupture discs. The He venting through the insulation space scattered insulation through the transfer hall. The He gas return line was still being pumped. The actual cause of the LHe bore tube collapse and rupture may never be known but it does appear that it was not caused by an increase in heat load due to the He gas return line leak, as the line was still being pumped on and under vacuum after the accident occurred.

Disassembly of this doublet showed that the LHe container bore tube ruptured next to the weld at the container end plate as shown in Fig. 5. The LN2 cooled shield had sustained some deformation and much of the insulation blanket around the shield had been shredded. Little damage to the device immediately next to the doublet could be noticed as viewed through the cryogenic manifold which was open after the doublet was removed. It is still not determined what effect the accident had on the other devices using the common insulating vacuum. Based on the shield deformation in this doublet, the shield deformations on the other cryostats involved should not effect operation but the condition of the other insulation blankets is not yet known. Some of the devices in that section have been cooled and operated normally but the degree of cryogenic efficiency was not determined because of the construction schedule.

An investigation of this incident was done including the use of two outside consultants, R. Powers of Powers Associates, Inc., and J. Purcell of Advanced Cryomagnetics. Results have prompted design changes and procedures for present and future cryogenic devices.

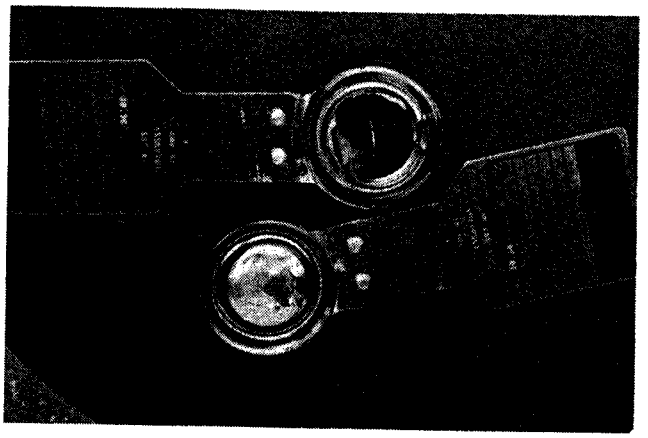

Fig. 4 Rupture discs from doublets involved in LHe container rupture incident. The lower disc is from the vent on the ruptured LHe container.

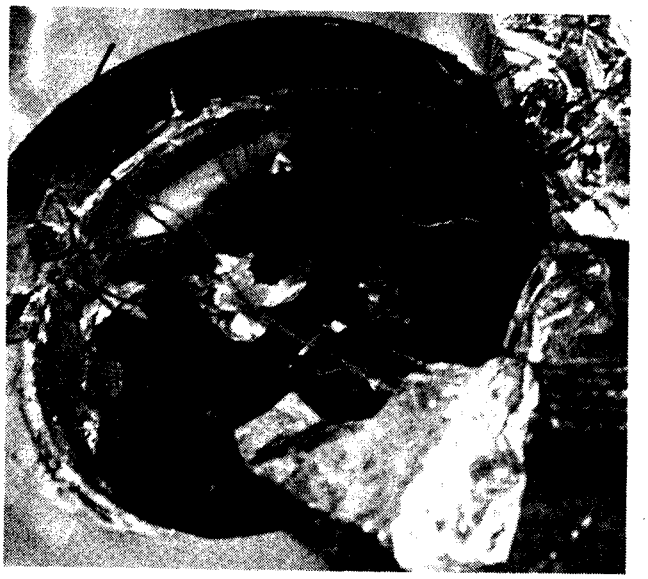

Fig. 5 Ruptured area of doublet LHe container.

Superconducting Beamline Magnet Design Changes

Each magnet cryostat will have a 3 in. (7.6 cm) dia. lift disc installed which opens at 2 psi or lower differential pressure. The large unobstructed orifice helps to prevent plugging with insulation and insures adequate flow capacity during a LHe container rupture. The popoffs originally considered are too restrictive for this condition. Also, a minimum of 2 lift discs will be present on each isolated cryostat vacuum section.

The maximum operating pressure of the magnet LHe containers will be lowered from 45 psid to below 35 psid. This should help to increase the margin of safety against bore tube collapse in the quadrupoles. A single element type disc which does not need a separate vacuum support will be used as the secondary He relief. A primary He relief of the spring loaded type is being added which opens at 27 psid (12 psig). A pressure control valve in the present design will have it's set point lowered from 30 psid to 23 psid (8 psig).

Future container designs will have more attention paid to critical joints with stiffening added if needed, and designs will follow the ASME pressure vessel code whenever possible. Heat shields within the cryostat will also be stiffened as necessary; baffled ports will be added to help prevent shield deformation due to differential pressure. These changes have already been incorporated into the triplets under construction.

Triplet Design and Construction

The quad triplet cryostat design closely follows that of the quad doublet[3]. The LN2 container is identical as extra holding capacity is not necessary. The LHe container and vacuum vessel are 12 in. (.3 m) longer since the magnet assembly is longer. Stiffening rings are being added to the magnet bore tube between each magnet and at the joints to the container ends. The magnet assembly consists of 1 NSCL standard beamline quad between 2 half length quads. The half quad is identical to the standard quad except for length. A triplet magnet assembly is shown in Fig. 6. All cryostat parts have been received and construction is already underway.

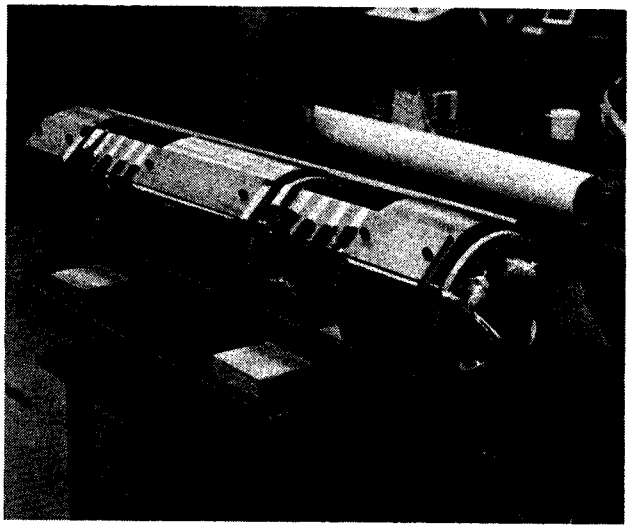

Fig. 6 Quad triplet magnet assembly showing 1 full length quad between 2 half length quads.

References

1. J.C. DeKamp et al., MSU Annual Report, 1988, 157.
2. B. Sherrill et al., MSU Annual Report, 1987, 190.
3. J.C. DeKamp et al., MSU Annual Report, 1987, 187.

SUPERCONDUCTING BEAMLINE QUADRUPOLE HARMONIC CONTENT

A. Zeller, J. DeKamp, C. Magsig, J. Nolen, and D. Tymes

All of the beamline quadrupoles, except for the prototype, were made from pole tip and yoke assemblies procured from Japan Steel. Previous measurements of the uniformity of the gradient were done on the prototype[1] which had a known pole tip error. This resulted in a sextupole error of about 2 part per thousand of the quadrupole field. All of the inspection reports on the production iron assemblies showed that the machining errors were five times less than those in the prototype assembly. Because of the timescale involved in installing the beamline, no further magnet assemblies were mapped while cold. However, two of the assemblies were mapped at room temperature.

Because of the large resistance of the coils at room temperature, only 40 mA of current could be used. This produces approximately 30 Gauss at the pole tips. Since the calculated gradient uniformities[2] change little in the excitation range where the pole tips are not saturated, this is sufficient current to compare with the infinite permeability calculations. Additionally, the mapper assembly has some mechanical tolerances which allow the mapper arm to rotate in an eccentric manner. To determine the effect of this rotation, the warm assembly was rotated by 90 degrees and remapped. Comparing the two maps allows us to remove the component of the field which is due to the mapper. The maps were taken with the coils arranged in a bucking geometry which reduces the dipole and quadrupole signals by a factor of 250. The raw data were smoothed and interpolated to give a uniform angular step size for Fourier analysis.

Fig. 1 shows a map of quadrupole number 4. The raw data is shown along with the mapper error and the resulting map which has the mapper error removed. The harmonic content of both quadrupoles for a radius of 1.5" are given in Table I. Note that only the N=6 and 10 terms are allowed, the rest of the terms result from mechanical errors. The uncertainties are the range of values obtained from both orientations of the quads. Error terms not listed are less than 0.01 parts per thousand of the quadrupole field. Dipole errors cannot be determined by this procedure, since the quad and dipole fields have been removed with the bucking coils; any dipole error which may exist is compensated for by aligning the quadrupole field to coincide with the beam axis.

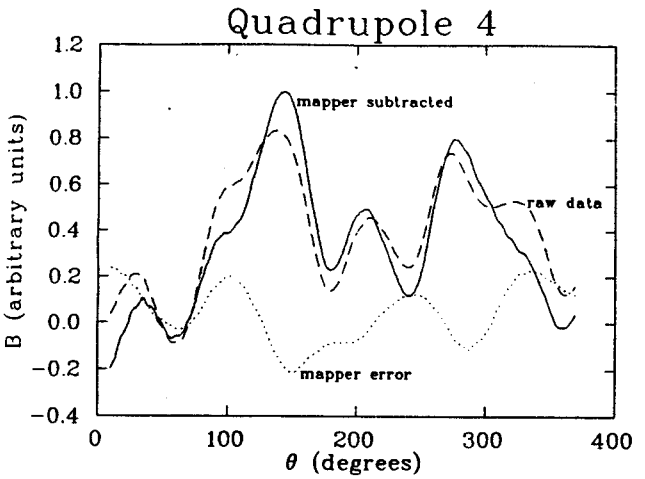

Fig. 1 Magnetic field as a function of angle for quadrupole #4 at room temperature. The main quadrupole field has been "bucked out" so only the error terms remain. The dashed line is the raw data, and the dotted line the mapper error. Subtracting the mapper error results in the solid line, which is the error due to the quad itself.

POISSON calculations for the infinite permeability case predicts the N=6 and 10 terms to be 0.25 and 0.01 $X10^{-3}$ of the quad field at 1.5" radius, in good agreement with the measured values. Both of these quads have much lower "construction error" terms than the prototype

quad[1] which has N=3 and 4 components of 1.8 and 1.2 $X10^{-3}$, respectively.

Table I

Multipole content of beamline quads at 1.5" radius and 30 Gauss pole tip field.

Quad	N=3	4	5	6	7	10
		($X10^{-3}$ of the N=2 (quad field))				
1	0.29±.05	0.31±.05	0.18±.02	0.28±.08	0.05±.01	0.03±.01
4	0.27±.09	0.20±.02	0.09±.02	0.33±.03	0.03±.01	0.03±.01

Note: The number of poles is 2 times N.

References

1. A.F. Zeller et al, MSU An. Report,176(1985).
2. A.F. Zeller et al, Proc. Ninth International Conf. on Magnet Technology,160(1985).

K1200 DEFLECTOR DEVELOPMENT

T. Kuo and J. Nolen

Introduction

The beam with the highest electrical rigidity from the K1200 cyclotron will be the 200 MeV/A q/A=0.5 ions. This beam will require the 2 deflectors, E1 and E2, to run at a voltage of 80 kV with a 6 mm gap. To date beams have been run which require deflector voltages of 40-50 kV. As higher voltages are required, the deflectors will have to be improved to make operations smoother. A summary of the present situation and identified problem areas together with development plans are presented below.

Initial Performance and Difficulties

The basic difficulties are sparking and excessive leakage current at relatively low deflector voltages. As mentioned above, early operation in the K1200 has been in the 40-50 kV range, with some conditioning problems in the upper end of this range. At pressures of 10^{-6} torr in the cyclotron the deflector leakage currents tend to rise to above 200 μa at about 50 kV. These currents can usually be reduced by leaking air or argon into the vicinity of the deflector. The leak makes only a small increase in the average beam chamber vacuum. The deflectors could be conditioned to voltages well above 50 kV with the cyclotron magnetic field off, but they ran only at lower voltages with the field on.

With the magnetic field on the sparks have their energy concentrated in small spots on the tungsten sparking plates above and below the cathode. The damage to these plates and the related metalization of other components deteriorates deflector performance and requires cleaning and sand blasting to renew performance.

The insulators sometimes give problems in a more random way, but usually only at voltages of 80-90 kV. They are often the limiting phenomena in a separate test stand, where the magnetic field is limited to 1T, rather than the 5.5T in the cyclotron.

Minimizing the Damage from Sparking

We were informed by Bob Rogers of Texas A&M Cyclotron Institute that they have used a resistive feed cable of several hundred kilo-ohm and obtained good results. The reasons for the improvement seems to come from the fact that a large portion of the discharge energy is dissipated in the cable and that the time constant of the discharge increases substantially. These two factors should then decrease the pitting of the tungsten ground plates and lessen the amount of tungsten droplets flying off to the negative electrode. The deflector can therefore be conditioned to hold a higher voltage than can be obtained with a non-resistive cable. (External "surge" resistors have been used at the K500 cyclotron for years, but they are not nearly as effective and easy to use as the resistive cable.) Recent tests using the resistive cables with E1 and E2 for the first time permitted holding voltage up to 80 kV. Beyond this, the support insulators broke down. The damage on the sparking plates was much less severe than before.

We were informed by the Milan group that molybdenum might be a better metal for the sparking plate than tungsten. We shall investigate the performance of Mo and possible other sparking plate materials in our test facility.

Minimizing the Leakage Currents

1. Surface Coating

Deflector discharges occur mostly between the negative electrode and the ground plates due to the vertical magnetic field. If one wants to minimize the frequency of discharge, one has to suppress the electron emission from the negative electrode. Dielectric surface coating on the negative electrode seems to be promising, but new problems can occur when a coating is used. For example, beam hitting the negative electrode could damage the coating material.

With the cooperation of Dr. Barasch from Texas A&M, a cylindrical disk was painted with green HV insulating varnish and subsequently put under test. It held 90 kV with a 5 mm gap for a week without a single discharge using our discharge-free feedthrough. However, firm conclusions are difficult because similar results can sometimes be obtained with a bare disk. Furthermore, it seems unsuitable to put organic compounds in a cyclotron environment and subject it to RF heating and beam bombardment. Atlernatively, anodized aluminum and titanium disks have been prepared at Sandia National Laboratory for us. These will be tested and results will be used to determine whether a full size deflector negative electrode should be coated as the next step.

2. Supporting Insulator

At present all supporting insulators are made of sapphire. Unlike alumina it is believed that the crystal structure is uniform and thus free of local voids. Recent observation of the failure mode of the deflector under test indicated that the sapphire might glow at 50-60 kV bias voltage with large leakage currents. This phenomenon looks like sparking if the insulator glowing is not visible. Further tests indicated that the voltage holding capability might have an orientation preference and that the breakdown voltage varies at different test intervals. This might explain some unpredictability in deflector performance.

While we are doing more tests to understand this particular problem, other insulating materials such as Macor are being considered. Several methods of brazing titanium to Macor are being investigated.

3. Insulator Mounting

In addition to the volume effect, frequent discharges over the surface of the sapphire insulator have been observed. This is consistent with the observation that the insulators removed from K1200 cyclotron are found coated with a metallic film at the high voltage end. Also, the metallic layer at the brazing joint was depleted around the outer rim. The metallic coating might come from the evaporation of brazing compound due to discharges at the joint. It is also noted that arcing tracks and a brown strip were present on only one side of the insulator at the level of cyclotron median plane. One might infer that this phenomenon stems mainly from the ExB electron drift effect. Secondary electrons are emitted from the insulator due to these ExB electrons and a positively charged track is created resulting in a flashover from the high negative voltage end to the grounded end.

Tests have been conducted to search for an alternative insulator mounting technique to minimize these flashovers. Using a special test electrode, the sapphire insulators were positioned above or below the midplane, allowing the midplane ExB electrons to pass through without hitting the insulators. Corona cups which protect the brazing joint and make the mounting interface less critical were also added at the HV ends. The combined result of these two techniques was quite successful. No flashover was observed along the sapphire insulator up to 95 kV for a long testing period. Tests to further confirm this improvement will

be conducted and the feasibility of adopting the structure to the actual deflector will be studied. (The geometry used for this test was not compatible with the space in the cyclotron.)

4. Magnetic and Gas Feed Effect

In tests of E2 deflectors in the test stand, the discharge frequency was found to depend strongly on the magnetic field strength. When no magnetic field was applied, the E2 deflector was able to hold up to 100 kV with only moderate leakage current, but the discharge frequency and leakage current increased as the magnetic field was increased. It was also found that the degree of damage became worse with increasing magnetic field. This means that good results obtained from the test stand might not be applicable to the higher magnetic field situation in the K1200 cyclotron. A side-by-side test of magnetic field effects using two E2 deflectors in the K1200 is planned. These two deflectors will be prepared identically, one will be tested at ~0.8T and the other at 5T field. The result will give a direct comparison of damage at two magnetic fields in the actual operating environment.

It is common practice to send gas to the deflector to suppress discharges. Tests are being conducted to determine what kind of gas is most effective. At the present time we use mainly Ar and air, with the results for these two gases being not too different. Helium gas seems less effective in our system. The quantity of gas to be used and the way of feeding are also being studied to minimize the effect on the cyclotron vacuum.

Summary

In the preceding paragraphs, we have described the major difficulties associated with the K1200 deflector of the present design in terms of hardware and physical phenomena. Certain possible solutions are proposed and will be tested using our test facility. Modifications to the present design within the constraint of fitting them to the cyclotron will be made as soon as the results of the tests are confirmed. Other issues such as methods of deflector cleaning and handling, testing and voltage conditioning procedures, quality assurance and documentation, etc., will be reviewed. Our goal is to reach 100 kV peak voltage capability so that stable operation at 80 kV can be routinely and reliably achieved.

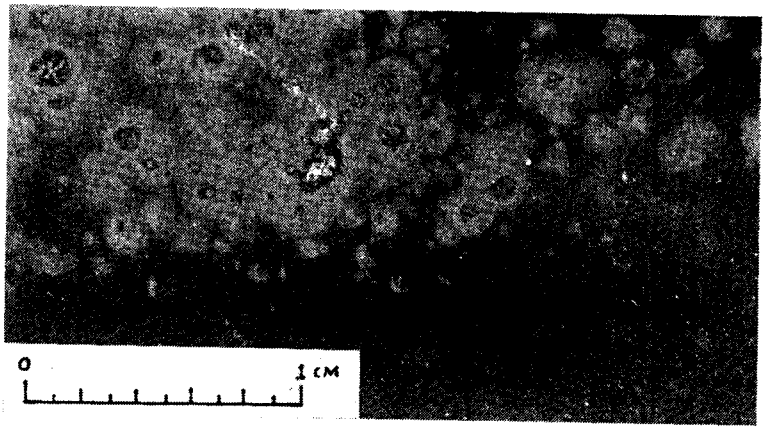

Image of EXB electrons' path along the surface of the HV negative electrode of the K1200 E2 deflector. The image was obtained during a test in the test stand. Heavy oil molecules were ionized by these electrons or by gas ions and then pulled down to the ground plate to make this imprint.

HIGH-T_c SUPERCONDUCTORS AS THERMAL RADIATION SHIELDS

A.F. Zeller

Most research in applications of high transition temperature (high-T_c) superconductors focuses on current transport and superconducting electronics. One potential application is in the area of thermal radiation shielding, an area which does not require high critical currents or fields. Although the use of a superconducting shield has been suggested before[1] as a radiation shield between 77 K and 4 K, only Nb_3Sn with a T_c of 18 K was available. This was not useful for shielding the 4 K surface from infrared radiation emitted from a 77 K surface.

The energy density, ρ_λ, at a wavelength, λ, of radiation emitted by a blackbody at a temperature T is given by the Planck Radiation Law:

$$\rho_\lambda = \frac{8\pi hc}{\lambda^5(e^{hc/\lambda kT}-1)} \qquad (1)$$

where h is Planck's constant, c is the speed of light, and k is Boltzmann's constant. Multiplying Eq. 1 by c/4 yields the emissive power per unit wavelength,

$$E_{b\lambda} = \rho_\lambda c/4 \ . \qquad (2)$$

The integral of Eq. 2 for λ=0 to ∞ yields the Stefan-Boltzmann Law, an energy transfer rate per unit area. For two surfaces at different temperatures, such as cryostats at liquid helium and liquid nitrogen temperatures, the radiative heat transfer per unit area, with a correction factor for non-blackbody emissivities, is where

$$Q/A = F\sigma E(77^4 - 4^4) \qquad (3)$$

where $\sigma = 5.67 \times 10^{-8}$ $Wm^{-2}K^{-4}$. E is the emissivity function defined as

$$E = \frac{1}{1/\varepsilon_4 + (1/\varepsilon_{77} - 1)} \qquad (4)$$

the subscripts refer to the surface temperatures. F is the configuration factor, which is assumed to be unity. Equation 3 is used here for parallel plates with equal and large areas. For emissivities of 1 the energy transfer rate is 2 W/m^2. The normal procedure is to use highly conductive materials of low emissivity for both the 77 and 4 K surfaces in order to reduce the heat transfer. Thus by the application of aluminum tape to the opposing 77 and 4 K surfaces in a stainless steel cryostat to produce emissivities of 0.03 and 0.011, respectively, Chaussy et al.[2] measured a thermal radiation transfer rate of 19.8 mW/m^2 without the use of superinsulation. Substitution of these emissivities into Eq. 3 predicts a heat transfer rate of 16 mW/m^2. In fact, better emissivities seem to be available, since Leung et al.[1] observe a rate of 12.4 mW/m^2 by using a different highly conducting aluminum tape on both surfaces. However, this probably represents the limit of what can be achieved by this method. Superinsulation also serves the same purpose as conducting surfaces, but frequently represents a solid conduction path between surfaces, and is not any better than the reflecting surfaces.[1]

According to the Bardeen-Cooper-Schrieffer (BCS) theory[3] of superconductivity, a superconductor absorbs only photons of energy greater than the energy gap between the superconducting band and the normal band. The energy gap is given by

$$E_{gap} = hc/\lambda_c = 3.5\ kT_c \qquad (5)$$

at T=0 K. Thus for $\lambda_c > hc/3.5kT_c$ a superconducting coating on the 4 K surface is a

perfect reflector. For maximum efficiency the 4 K surface must be the one coated with superconductor. The energy gap decreases as $(1-T/T_c)^{1/2}$, so for a 90 K superconductor at 77 K λ_c must then be greater than $hc/1.2kT_c$. Figure 1 shows the radiation spectrum for a blackbody at 77 K as a function of wavelength, as well as the wavelengths where $\lambda=hc/3.5kT_c$ for several superconductors. All wavelengths longer (to the right of the vertical lines) are not absorbed. Integration of the spectrum to the absorption edge yields the effective heat transfer coefficient, σ', which is defined by

$$\sigma' = \frac{\int_0^{\lambda_c} E_{b\lambda}\, d\lambda}{\int_0^{\infty} E_{b\lambda}\, d\lambda} (77^4 - 4^4) \qquad (6)$$

Values of the coefficients corresponding to several known superconductors are given in Table I, which also shows, for comparison, the value corresponding to a hypothetical (but not unreasonable) superconductor with a T_c of 150 K. These values are calculated assuming each surface to be a blackbody (ε=1) and, therefore represent the maximum possible heat transfer rate between two surfaces. However, the 77 K surface can be a highly conducting such as aluminum with an $\varepsilon \leq 0.03$, so the heat transfer

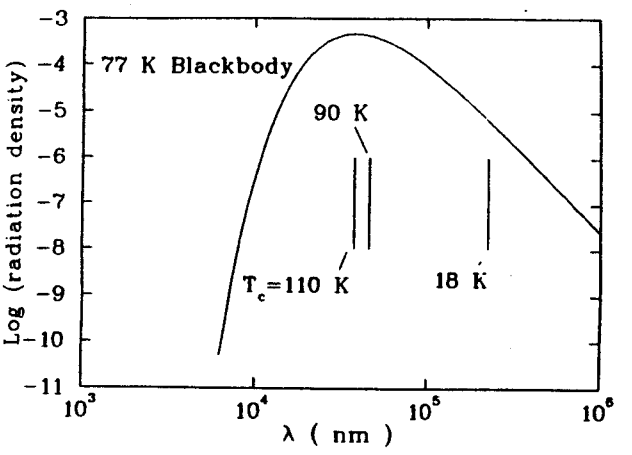

Fig. 1 Blackbody radiation spectrum for a surface at 77 K. Absorption edges for superconductors with the indicated T_c's are shown as the vertical lines. Note that the wavelengths to the right of each line are completely reflected.

rate for the 110 K superconductor would be 15 mW/m². If the 4 K surface has even a moderate emissivity of ε= 0.1, the heat transfer rate is further reduced to < 12 mW/m². Note that the emissivity of the 77 K surface (0.03) becomes the dominant factor in determining the final rate, since reducing the emissivity of the 4 K surface from 1 to 0.01 reduces the rate by only a factor of four. Therefore, reducing the emissivity of the 77 K surface from 0.03 to 0.02 reduces the rate to 10 mW/m² for a 4 K surface coated with a 110 K superconductor that absorbs as a blackbody for wavelengths shorter than λ_c.

TABLE I
Absorption characteristics for 77 K blackbody radiation.

Material	T_c(K)	λ_{min}(nm)	reflection(%)	ε_4 1 σ'(mW/m²)	$\dot{Q}/A, \varepsilon_{77}$=.03 (mW/m²)
Nb_3Sn	18	2.25×10^5	2	1960	59
$YBa_2Cu_3O_7$	90	4.57×10^4	61	780	23
Bi-Ca-Sr-Cu-O	110	3.74×10^4	75	500	15
Hypothetical	150	2.74×10^4	92	160	5

Therefore, coating the cold surface with a high-T_c superconductor, by plasma spraying for example[4], provides the means for reducing the radiation load on low loss cryostats. The observed[4] deterioration of the magnetic properties of $YBa_2Cu_3O_{7-x}$ when cycled ten times between 77 K and room temperature in air indicates the ceramic superconductors' sensitivity to moisture. Practical shields would need protection from moisture by hermetic sealing or exposure to only dry air. For cryostats surrounding a superconducting magnet, the fringe fields will cause the reflectivity to revert to its normal conducting state when the critical field is exceeded. The reduction in reflectivity depends on the field level and the extent of the field penetration into the superconductor. In thin films and in Type II superconductors the flux penetrates the superconductor but does not destroy superconductivity until the upper critical field is exceeded. The upper field is also temperature dependent, so high T_c superconductors at 4 K have significantly higher critical fields than at 77 K. Of course, the change in reflectivity in high magnetic fields for a given coating thickness would have to be measured. Certainly, the surface provides magnetic shielding for low magnetic fields[4]. Such shields, providing both magnetic and thermal radiation shielding, would be especially useful for spaceborne applications where exposure to the degrading effects of moist air would not be a problem.

References

1. Leung,E.M.W., Fast,R.W., Hart,H.L. and Heim,J.R., Adv Cryog Eng 25,489(1980).
2. Chaussy,J., Gianese,P. and Peyrand,J., Cryogenics 16,617(1976).
3. Bardeen,J., Cooper,L.N. and Schrieffer, J.R., Phys. Rev. 108,1175(1957).
4. Karthikeyan,J. et al, Cryogenics 29,915(1989) and references therein.

CENTRAL REGION CALCULATIONS FOR A 250 MEV SUPERCONDUCTING SYNCHROCYCLOTRON

X. Y. Wu and M. M. Gordon

Introduction

A 250 MeV superconducting synchrocyclotron being developed here for use in cancer therapy has a central field of 56 kG and a pole radius of 53 cm. Preliminary measurements indicate that an ion source chimney with a diameter of only 3.2 mm can produce a 2 mA current, and based on these results, an electrode configuration for the source-puller and dee geometry has been designed to provide the maximum phase acceptance consistent with adequate vertical focusing.

Central Region Design

The overall design of our central region geometry was influenced by the central region design of the CERN 600 MeV machine.[1] Since our central field is about three times stronger than the CERN machine, we have a much smaller space to use. The main components are two semi-cylindrical electrodes in contact with the dee and dummy-dee, respectively, to define the electric field. The puller is fixed to the dee-side electrode facing the source chimney and is inclined by 30° to the acceleration gap to compensate for the initial electrical phase shift of the injected protons. The source chimney has outer and inner diameter of 0.125 in. and 0.095 in.

Initially we used a 2 mm gap from the source to the puller and a 4.0 mm by 0.5 mm slit in the chimney, which makes the average electric field 100 kV/cm, since the dee voltage used here is 20 kV. Because the output ion current from the source is proportional to the electric field applied on the surface of the plasma, a stronger electric field is favored here. Based on the experience of operating the K100 superconducting cyclotron, the average peak electric field could reach as high as 150 kV/cm and a circular hole on the chimney will give a much higher output ion current than a rectangular slit. Therefore we reduce the gap from 2 mm to 1.5 mm and change the slit to a hole with a diameter of 0.75 mm and an open angle of 120°. Figure 1 shows the peak electric field distributions along the center line of the slit before and after the change. The peak electric field on the plasma surface has been increased from 63 kV/cm to 103 kV/cm. The change also decreases the transit time in the source to puller region.

The proposed vertical dee aperture is 0.6 inches. Preliminary orbit calculations indicate that the electric vertical focusing force is not strong enough if we use the symmetric dee and dummy-dee apertures about the center of the gap. In order to get some extra vertical focusing force, we used different entrance and exit apertures of dee and dummy-dee. The entrance aperture of dee or dummy-dee is 0.825 in. and the exit aperture is 0.525 in. Figure 2 shows the acceleration gap with symmetric and unsymmetric dee and dummy-dee apertures.

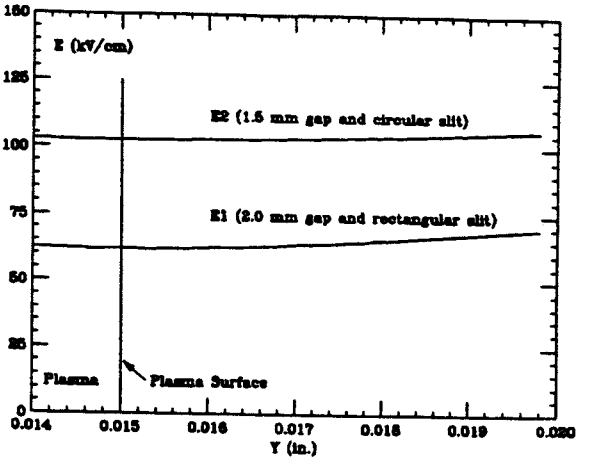

Fig. 1 Plot of electric field distributions in the center of chimney slit for 2 different cases, one with 2 mm source to puller gap and 4.0 by 0.5 mm² rectangular slit, and the other with 1.5 mm gap and a circular hole with diameter of 0.75 mm and an open angle of 120°.

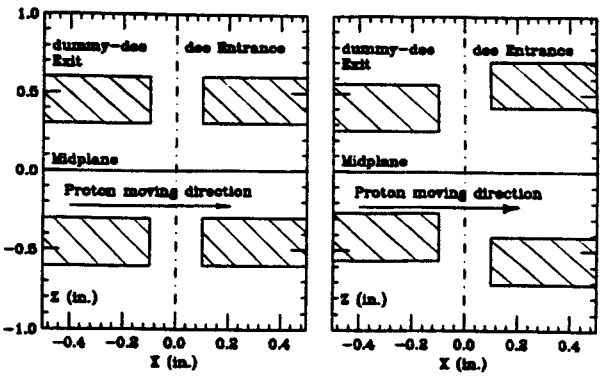

Fig. 2 Plot of cross section of the acceleration gap with the symmetric and unsymmetric dee and dummy-dee vertical apertures.

Orbit Calculations

The first part of the orbit calculations were performed using Parts I and II of our code CYCLONE. Part I integrates the equation of motion from source to puller in a fine electric field grid and part II continues for a few more turns in a coarser grid. Since the number of revolutions in synchrocyclotrons is very large, a transfer matrix code was developed to continue the orbit computations to full energy.

The electric potential maps were prepared with TRIUMF's RELAX3D4 code. Our grids for the small electric field between source to puller region are 121 by 121 points with a mesh size of 0.001 in., and the grids for the large electric field are 121 by 121 by 12 points with a mesh size of 0.015 in. and with planes parallel to the median plane 0.0375 inches apart.

Orbit Properties and Discussion

In designing the central region, we first want to maximumize phase acceptance. Those orbits starting at the ion source with times close to the central ray starting time should clear all the posts that go through the median plane that are used to define the electric field and the back of the source chimney. Secondly, we want the electrodes to provide adequate electric vertical focusing for all the orbits to avoid vertical beam loss, especially for the first few turns. Finally, we want all the orbits to be well centered and with radial oscillation amplitudes limited within an acceptable range.

The central ray starting time τ_o = 230° has the maximum energy gain after the acceleration from source to puller while the peak electric field is reached at τ_o = 270° . In Fig. 3, we have plotted 8 orbits for ions starting at τ_o = 200° to 265° in the small electric field. In Fig. 4, we have a similar plot in the large electric field for the first few turns. All the orbits clear the puller electrode and gain enough energy after the first two gaps to clear the posts and the chimney. Figure 5 shows the centering error for the protons with τ_o = 200°, 230° and 260°. The centering error for all the orbits is about 20 mils. The location of the chimney slit has a strong influence on the orbit centering error.

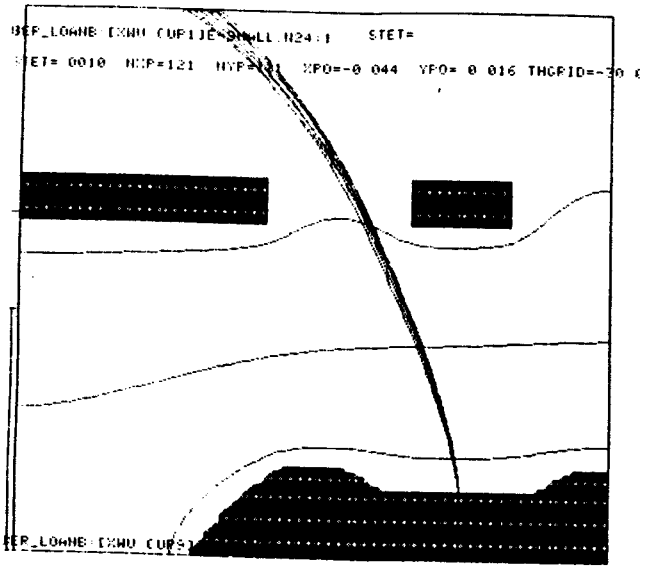

Fig. 3 Source chimney and puller electrodes in the median plane and equipotentials for the small electric field. 8 orbits are plotted, corresponding to starting time τ_o = 200° to 265°. The peak electric field between source and puller is achieved at τ_o = 270°. The central ray starting time is τ_o = 230°.

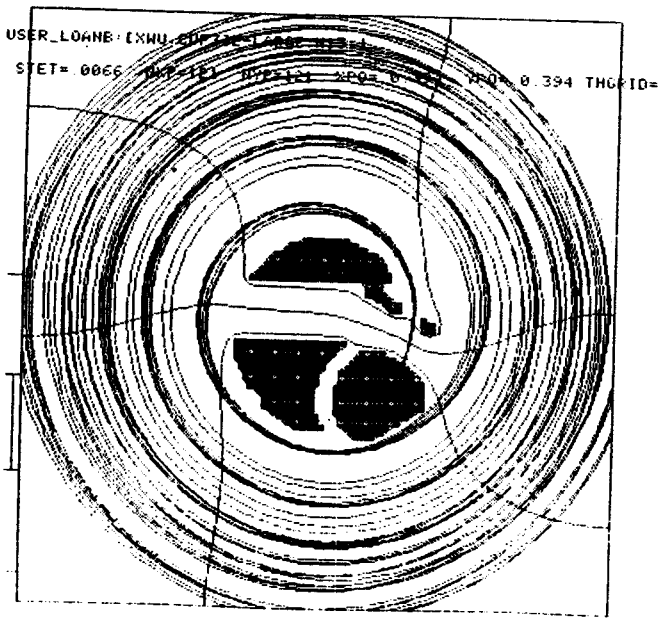

Fig. 4 Central region electrodes in the median plane and equipotentials for the large electric field. 8 orbits are plotted, corresponding to starting time τ_o = 200° to 265°.

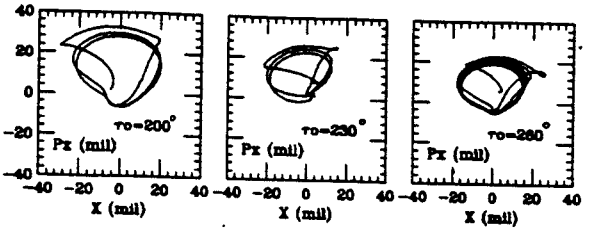

Fig. 5 Plots of x vs. p_x for protons starting at τ_o = 200°, 230° and 260°. The center errors for all the orbits are about 20 mils.

Figure 6 shows the average phases of the protons for orbits starting at τ_o = 200° to 265° for the first 20 turns. The average phase curve depends strongly on the starting time τ_o. Since the time term of the electric focusing force is proportional to sin(ϕ), the vertical motion of the orbit should also have strong dependence on the starting time τ_o. Fig. 7 shows the vertical motion for the starting condition (z,p_z) = (0.1,0.0) at the top, and for (z,p_z) = (0.0,0.01) at the bottom for protons starting at τ_o = 200°. In Figs. 8 and 9, we have similar plots for protons starting at τ_o = 230° and

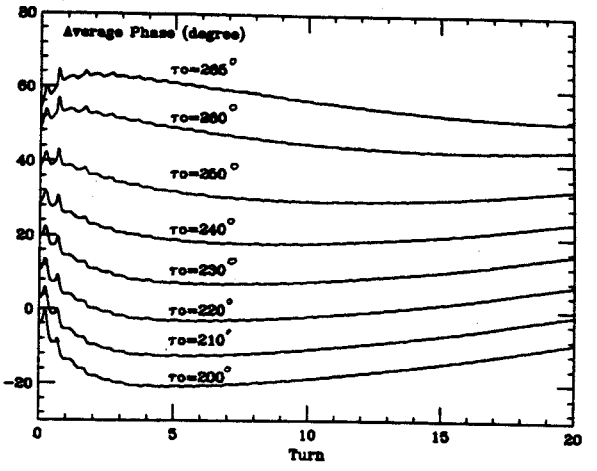

Fig. 6 Plot of average phase ϕ vs. Turns for protons starting at τ_o = 200° to 265° for the first 20 turns.

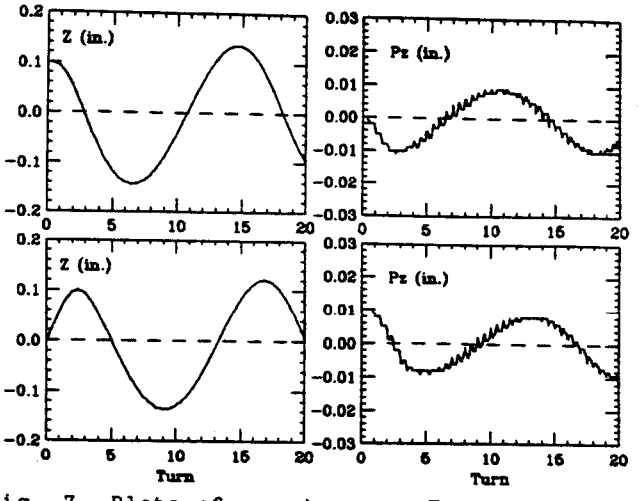

Fig. 7 Plots of z and p_z vs. Turns for the starting condition (z,p_z) = (0.1,0.0) in. at the top, and for (z,p_z) = (0.0,0.01) in. at the bottom with protons starting at τ_o = 200° at the source.

260°. We observe from the plots the strong dependence of the vertical focusing frequency on the protons' starting time τ_o and that the vertical oscillation amplitudes for all three orbits don't increase significantly for the first 20 turns. Since the electric vertical focusing is only important for the first few turns of the orbits and magnetic vertical focusing is dominant thereafter, the vertical focusing requirement is well satisfied.

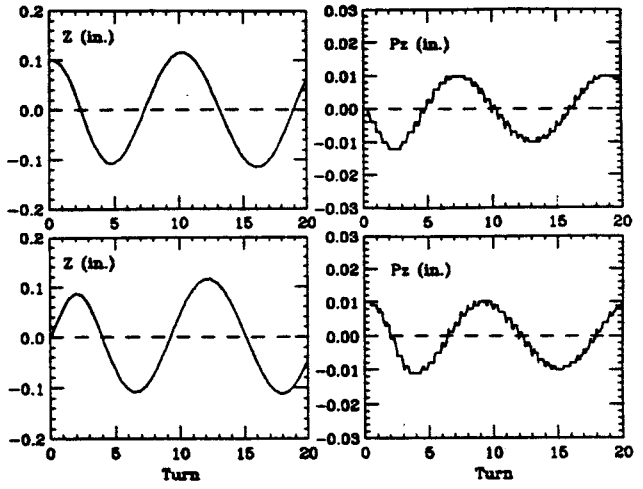

Fig. 8 Plots of z and p_z vs. Turns for the starting condition $(z,p_z) = (0.1,0.0)$ in. at the top, and for $(z,p_z) = (0.0,0.01)$ in. at the bottom with protons starting at $\tau_o = 230°$ at the source.

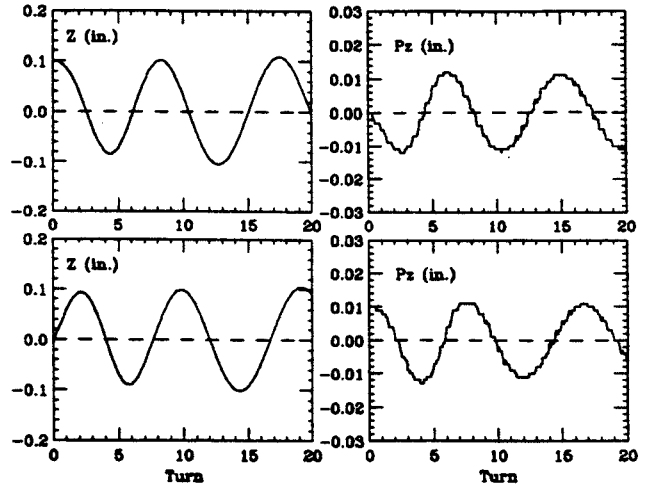

Fig. 9 Plots of z and p_z vs. Turns for the starting condition $(z,p_z) = (0.1,0.0)$ in. at the top, and for $(z,p_z) = (0.0,0.01)$ in. at the bottom with protons starting at $\tau_o = 260°$ at the source.

Reference

1. R. Galiana et al., Proceedings of the 7th International Cyclotron Conference (Birkhauser, Basel, 1975), p. 371-375.

THE 250 MEV SUPERCONDUCTING SYNCHROCYCLOTRON ION SOURCE EXPERIMENT

X. Y. Wu, H. Blosser and T. Kuo

Introduction

The proposed K250 superconducting synchrocyclotron has a high central magnetic field of 56 KG and a small pole radius of 53 cm. The strong magnetic field leaves very limited space for the cyclotron ion source and central region electrodes. Studies of the extraction system for this cyclotron show that good internal beam quality is required in order to avoid the $\nu_r = 2\nu_z$ coupling resonance which leads to severe beam loss. The required control of the internal beam quality depends ultimately on the design of the central region and, in particular, on whether a "closed" ion source (i.e. an ion source with an enclosed plasma and a well defined exit slit) plus puller can be accommodated within the limited space available.

Initial studies of central region orbits in the 250 MeV superconducting synchrocyclotron show that an enclosed ion source plus puller is possible provided the ion source chimney is about 0.1 in. in diameter and the gap between the chimney and the puller is about 1 to 2 mm, and with dee voltage 10 to 20 KV range. With these requirements, a major experimental question then needs to be answered. Namely, can we extract enough ion current from an ion source with a 0.1 in. diameter chimney so as to have adequate beam current surviving the beam losses in the capture and extraction processes?

In order to answer this question and test the current K100 cyclotron ion source behavior under similar operating conditions, we did an experiment to measure the total ion current of the K100 superconducting cyclotron ion source in comparison with that of a modified, small chimney, version of this source. The experiment consisted of two parts, namely, in test #1, we measured the ion current of the K100 cyclotron ion source, using the 0.250 in. diameter chimney, which is currently used in the K100 central region, and in test #2, we measured the ion current of the K100 cyclotron ion source, using a 0.125 in. diameter chimney, which is the standard tubing nearest to the size of chimney proposed for the K250 superconducting synchrocyclotron central region. The K100 superconducting cyclotron has a central magnetic field of 46 KG and deuterons were used as the test ion because of the existing K100 gas system.

Ion Source Experiment Setup

In order to put in the pullers and the supporting system, we take the spider in the K100 Cyclotron central region out. Fig. 1 shows the schematic diagram of experiment setup, and Fig. 2 shows the cross sections of the central region with puller and supporting system in place for the tests.

The different geometric parameters used in test #1 and #2 are listed in table I.

Table I

	Test #1	Test #2
Chimney I. D. (in.)	0.220	0.095
Chimney O. D. (in.)	0.250	0.125
Slit Width (in.)	0.020	0.020
Slit Length (in.)	0.220	0.160
Slit Area (mm^2)	2.840	2.065
Puller I. D. (in.)	0.369	0.243
Puller O. D. (in.)	0.539	0.394
Gap (mm)	1.500	1.500

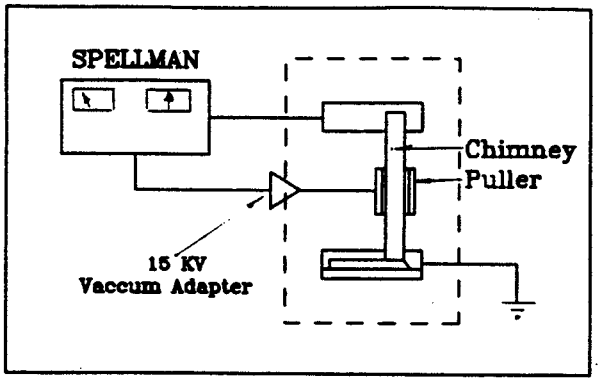

Fig. 1 -- Schematic diagram of ion source experiment setup.

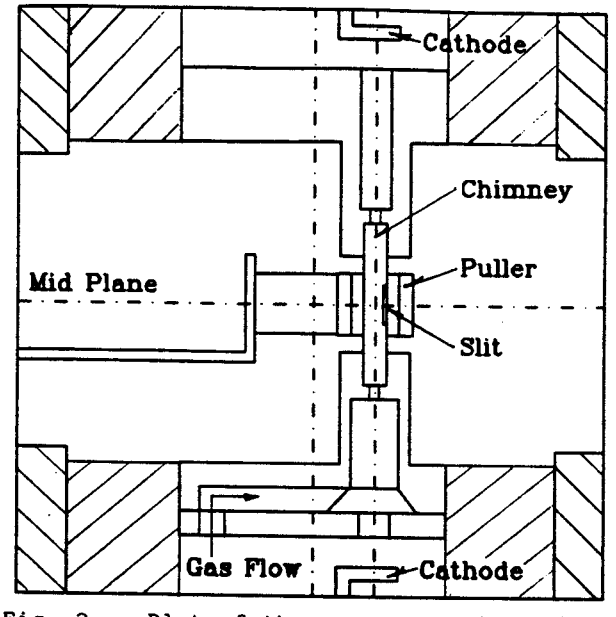

Fig. 2 -- Plot of the cross section of the central region with puller and supporting system in place for the test. The diameter of the chimney is 0.250 in. and 0.125 in. respectively.

The cylindrical puller and supporting copper connector are mounted on an insulator (Boron Nitride) which is fixed on one of the magnet hills. They are connected to an RG 213 /U cable. The cable goes through the K100 cyclotron target hole and a 15 KV Vacuum Adapter and connects to a SPELLMAN RHR 15N120 high voltage power supply, which can provide -15 KV peak DC voltage.

Experiment Result and discussion

(1) In test #1, we measured the ion current of the K100 cyclotron ion source, using the 0.250 in. diameter chimney, which is currently used in the K100 central region. Fig. 3, 4 and 5 show the 3 different ion current measurements.

(2) In test #2, we measured the ion current of the K100 cyclotron ion source, using the 0.125 in. diameter chimney, which is very close in size with the chimney proposed to be used in K250 superconducting synchrocyclotron central region. The calculation results of the K250 superconducting synchrocyclotron show that it requires a 0.095 in. diameter chimney. Fig. 6 and 7 show the 2 different ion current measurements in test #2.

Result Analysis and Conclusion

We calculated the electric fields between the chimney and the puller region for both test #1 and #2 geometries. The electric field distributions along the center line of the chimney slit are shown in Fig. 8 for both test #1 and #2 with different extraction voltages and with no conducting plasma in the chimney. Results show how the electric field penetrates into an empty chimney with different extraction voltages. The wall thickness of the chimney in the center of the slit is 0.010 in. for test #1 chimney and 0.005 in. for test #2 chimney. These are also shown in Fig. 11. Line A and Line C show the inside and outside boundary of the 0.250 in diameter chimney, and line B and line C are those of the 0.125 in. diameter chimney. Plasma in the chimney will of course modify these results but major trends should be the same.

The extracted ion current I_{ext} should be proportional to the cross section of the chimney and the electric field on the surface of the plasma. The cross section of the chimney in test #1 (0.220 in. inside diameter) is about 4 times of that in test #2 (0.095 in. inside diameter). The strength of the electric field at the inside diameter of the chimney in test #1, E_A, is only half of that in test #2, E_B, as is shown in Fig. 11. This is due to the different wall thickness of the chimney in the center of the slit. Combining these two factors, we should have $I_{ext1} = 2I_{ext2}$. Fig. 9

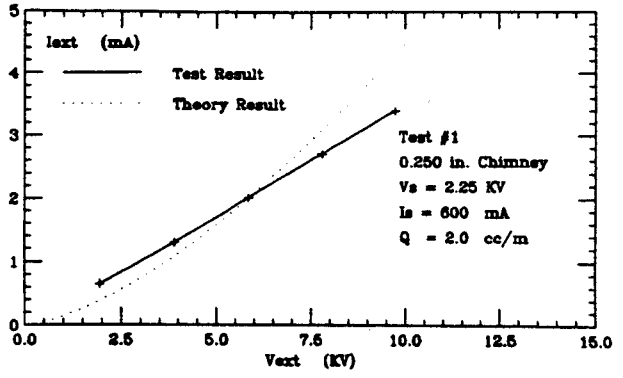

Fig. 3 -- Plot of ion current I_{ext} vs. extraction voltage V_{ext}. Also the theory curve is shown, using the simple model of $I_{ext} = AV_{ext}^{3/2}$, where A is a constant.

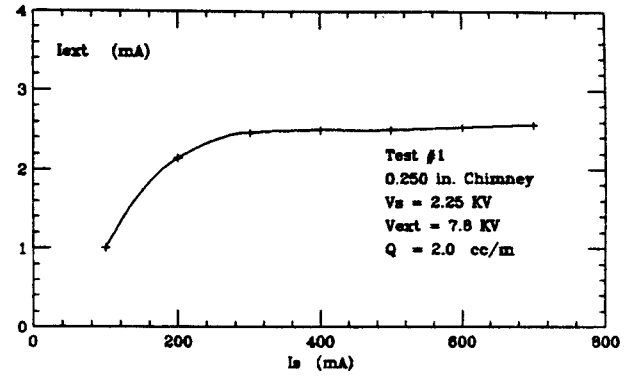

Fig. 4 -- Plot of ion current I_{ext} vs. source current I_s. With a constant extraction voltage V_{ext} = 7.8 KV, the ion current I_{ext} saturated when source current I_s reached about 300 mA.

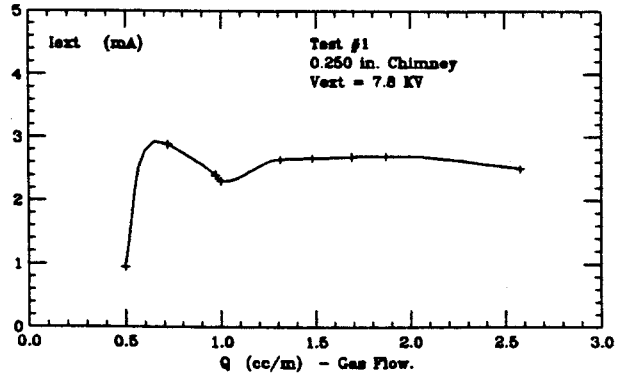

Fig. 5 -- Plot of ion current I_{ext} vs. gas flow Q. With a constant extraction voltage V_{ext} = 7.8 KV, the ion current I_{ext} saturated when gas flow Q reached about 1.25 cc/m.

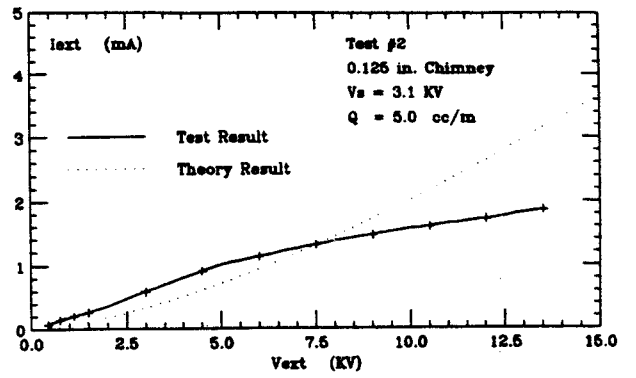

Fig. 6 -- Plot of ion current I_{ext} vs. extraction voltage V_{ext}. Also the theory curve is shown, using the simple model of $I_{ext} = AV_{ext}^{3/2}$, where A is a constant.

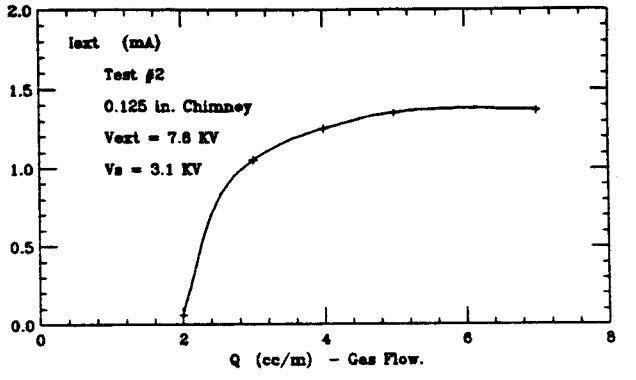

Fig. 7 -- Plot of ion current I_{ext} vs. gas flow Q. With a constant extraction voltage V_{ext} = 7.8 KV, the ion current I_{ext} saturated when gas flow Q reached about 4.0 cc/m.

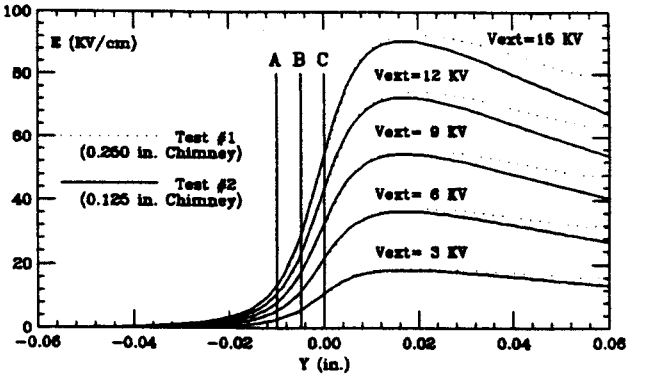

Fig. 8 -- Plots of electric field along the center line of the chimney slit in test #1 and #2 with different extraction voltage. Line A and line C are the inside and outside boundary of 0.250 in. diameter chimney wall, and line B and line C are those of 0.125 in. diameter chimney wall. No conducting plasma is assumed in the source.

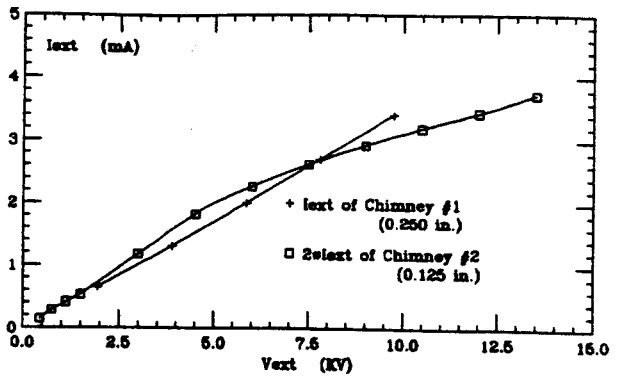

Fig. 9 -- Plots of I_{ext} in test #1 (0.250 in. diameter chimney) and $2I_{ext}$ in test #2 (0.125 in. diameter chimney) vs. the extraction voltage V_{ext}.

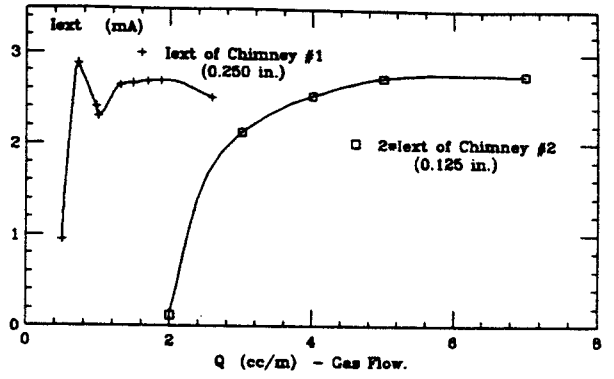

Fig. 10 -- Plots of I_{ext} in test #1 (0.250 in. diameter chimney) and $2I_{ext}$ in test #2 (0.125 in. diameter chimney) vs. the gas flow.

shows I_{ext} in test #1 and $2I_{ext}$ in test #2 as a function of extraction voltage, and we can see they agree with the argument quite well.

We find that the extracted ion current I_{ext} quickly increased as gas flow was increased, saturating very quickly with a constant extraction voltage in both tests. This agrees with the other source experiment results. Again the saturated ion current I_{ext} in test #1 should be twice of that in test #2, since the same argument also applied here. I_{ext} in test #1 and $2I_{ext}$ in test #2 are plotted vs. the gas flow in Fig. 10. Again we can see they agree with the argument well although the required gas flow is quite different in two different cases.

The peak extracted ion current obtained with 0.125 in. diameter chimney is about 1.85 mA when the extraction voltage was 13.5 KV. This certainly indicates that it is possible to obtain enough ion current from a central region design for K250 superconducting synchrocyclotron having an enclosed ion source with a very small diameter chimney, about 0.1 in., plus a puller. The ion source for K250 machine could be similar to the current K100 cyclotron ion source. The experiment result answers our original question. At the same time, we tested the current K100 ion source behavior under the similar operating circumstances, which provides us important information to understand the performance of K100 ion source and cyclotron.

IMPROVED FORMULAS FOR CALCULATING CYCLOTRON ORBIT PROPERTIES

M.M. Gordon and Dong-O Jeon

In determining whether a given magnetic field meets the performance requirements for accelerating a particular ion to a given final energy, one must calculate certain orbit properties from this field as a function of energy or radius. The most important of these properties are the orbit period τ and the radial and vertical tunes, ν_r and ν_z.

The required calculations are carried out using either analytical formulas or an orbit integration program known as the Equilibrium Orbit Code or one of its variants. The E.O. code is widely used and its accuracy is excellent, but its numerical results do not easily provide insight into the effects of various field characteristics on the results. Such insight is on the other hand readily available from analytical formulas.

Analytical descriptions of cyclotron orbit properties have been given by many authors in the past and although the resultant formulas have proved useful, their accuracy has been limited particularly when applied to machines with only three sectors. Noting this, we have undertaken the task of deriving more accurate formulas by introducing several improvements. First of all, our analysis systematically maintains all terms, whether large or small, that are of second-order in the flutter field, that is, the part of the field that varies with the azimuth θ. In doing so, we also utilize an improved first-order calculation of the equilibrium orbits themselves. Finally, the values of ν_r and ν_z are calculated from a formula which is derived from a second-order Born approximation and which should be valid all the way up to the stop-band limit, $\nu = N/2$, where N is the number of sectors.

Our formulas should work especially well for any superconducting cyclotron when the operating condition is close to the bending limit of the magnet. In such cases, the flutter field is relatively small so that the assumptions of the analysis are accurately justified. To test the analysis in a real situation we have investigated the Harper Hospital cyclotron which has a central field of 46 kG and is designed to accelerate deuterons to an energy of 50 MeV at a final radius of about 12 inches.

In order to judge the merits of our analytical formulas, we compare the results obtained from the Equilibrium Orbit Code with those obtained from the formulas by displaying the differences in the energy ΔE, the period $\Delta\tau$, and the tunes, $\Delta\nu_r$, and $\Delta\nu_z$, all as a function of the reference radius r_o. (The analysis uses radius as the independent variable and includes formulas for the momentum p and the energy E of the given ion as functions of radius for purposes of comparison, the Equilibrium Orbit Code was therefore modified to produce output at the same values of r_o.)

Figure 1 shows plots of $(\Delta E)/E$ and $(-\Delta\tau/\tau$ both in units of 10^{-5}, and it is clear that these fractional differences are very small for r_o<10 in.(33 MeV). For the last two inches (33 to 48 MeV), the magnitude of these quantities changes rapidly and erratically, and ends up about ten times larger than at the start. Moreover, the two sets of data follow the same general pattern with the values of $(\Delta E)/E$ being about twice those for $(-\Delta\tau)/\tau$.

Similar plots of $\Delta\nu_r$ in units of 10^{-4} and $\Delta\nu_z$ in units of 10^{-3} are both shown in Fig. 2. The values of $\Delta\nu_r$ are quite small and remain below 4×10^{-4} out to about 11 in., and then become very erratic in the last inch. The plot of $\Delta\nu_z$ follows the same general behavior, but the values are about five to ten times larger.

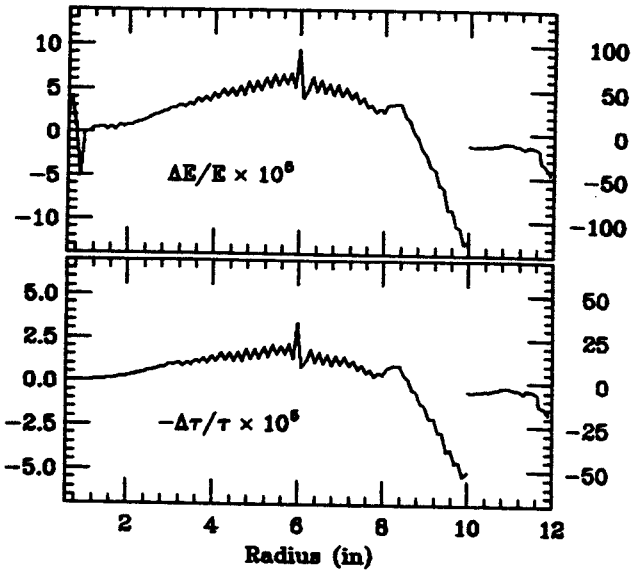

Fig. 1: Plots of (ΔE)/E at top and $(-\Delta\tau)/\tau$ at bottom versus radius for the Harper cyclotron. ΔE and Δτ are differences between the values obtained from the Equilibrium Orbit Code and from the analytical formulas. Both quantities are in units of 10^{-5} with the scale on the left being valid for r<10 in., and the scale on the right for r>10 in.

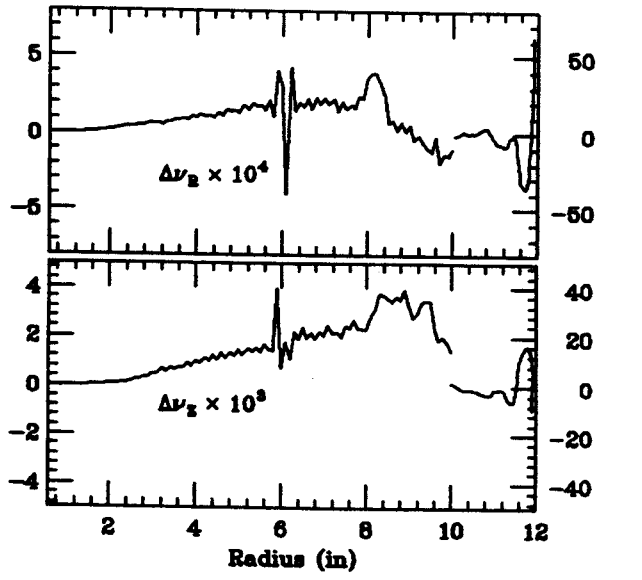

Fig. 2: Plots of $\Delta\nu_r$ in units of 10^{-4} at top, and $\Delta\nu_z$ in units of 10^{-3} at bottom, as a function of radius for the Harper cyclotron. Here again the scale on the left applies to r<10 in., and the one on the right to r>10 in.

This is not surprising since the theory involves ν_z^2, and one should therefore compare $\nu_z(\Delta\nu_z)$ with $\Delta\nu_r$. That is,, the values of ν_r always lie between 0.99 and 1.04, while the values of ν_z start out close to zero and then rise to a plateau with ν_z=0.2 between 9 and 11 in., and finally rise to 0.32 at 12 in.

All four of the plots described above show erratic behavior near 6 in., and between 10 and 12 in. This behavior can be traced to defects in the magnetic field data which we derived from field measurements. These defects are amplified in the process of taking differences between results from the Equilibrium Orbit Code and the analytical formulas. That is, the Equilibrium Orbit Code requires first derivatives in both r and θ, and must interpolate between the given data points. On the other hand, the analytical formulas require both first and second derivatives in r (and a third derivative of the average field), but do not use any interpolations.

The results so far clearly indicate that the analytical formulas are quite good. Moreover, comparisons like the one above reveal the limits on the accuracy of the output from the Equilibrium Orbit Code produced by small errors in the field data. We plan to carry out additional studies using field data from the K1200 cyclotron and from other cyclotrons, as well as fields derived from analytical formulas where difficulties associated with irregularities in the data can be avoided.

8-TESLA MAGNET FOR TEST STAND

J. Kim, J. Bailey, F. Marti, J. Nolen, H. Blosser

1. Introduction

We are planning to build a magnet for a multipurpose test stand. This magnet will be used to study interesting cyclotron related phenomena at high magnetic fields (≈8 Tesla) as well as at low fields (≈1.6 Tesla). Studies currently envisioned include design of central region components and inflectors, developing new cyclotron diagnostics, and determining both DC and RF voltage limits for various materials at various magnetic field levels. We will also be able to do many other interesting experiments with this compact magnet. This report describes the main features of the magnet and some of the details of the coil design.

2. Magnet Design

The Poisson code[1] was used to decide the main parameters of the magnet, which are shown in Fig. 1. One requirement in designing the magnet is low magnetic field strength (≤ 30 gauss) in the region beyond R=2 meters since strong magnetic fields interfere with the operation of other equipment (especially computers). Two options were available to meet this requirement, namely 1) use a reverse current coil on the outside of the yoke to compensate the field of the main coil, or 2) increase the yoke thickness to meet the requirement. Solution 1) can significantly reduce the iron weight as well as the outside field at the expense of a slight decrease of the inside field. However, the complicated coil system and higher cost were detractions. Solution 2), putting more iron in the yoke to lower the outside field, was selected, the lower total cost of the latter making it more attractive.

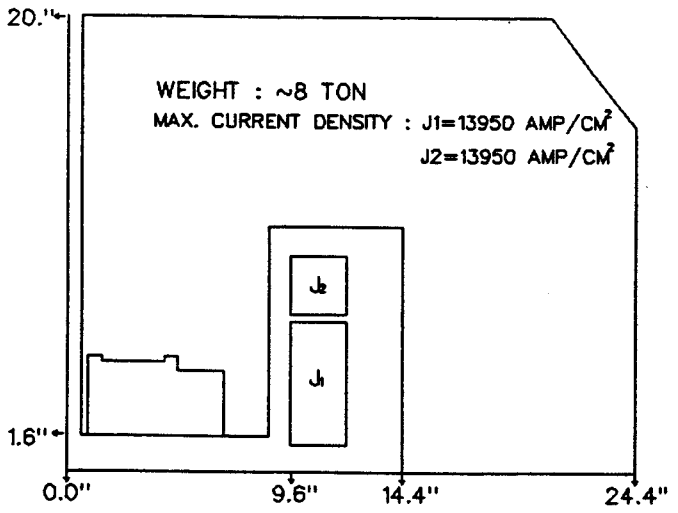

Fig. 1. Configuration and parameters of 8 Tesla magnet.

Another main issue in deciding the coil shape is to achieve a magnetic field which has an approximately flat radial dependence over the desired excitation range (1.6T - 8.0T); a two coil system will be used to accomplish this. Using this adjustment, radial field profiles at several excitation points as shown in Fig. 2 can be obtained.

3. Forces and Stresses

Overall forces on each coil were calculated with the Poisson code for two critical cases. Results are shown in Fig. 3 and give an indication of the average stress in each part of the coil. The forces approach 1000 tons and careful attention therefore needs to be directed to details of the stress inside the coil, since even tiny movements (≈0.01 mm) in a potted coil due to strong magnetic stresses can generate enough heat to produce a coil quench. The STANSOL program[2] has been used to obtain a more detailed picture of the stresses within the coil including winding preload and differential contraction from room temperature to 4K in

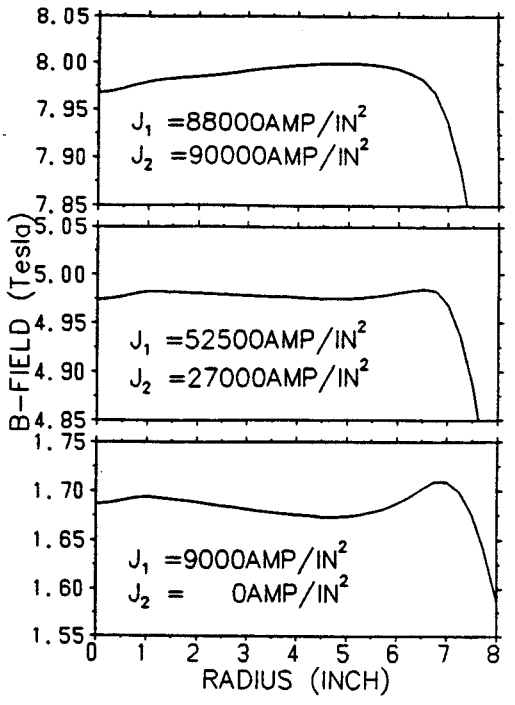

Fig. 2. B(r) at Z=0 for three excitations covering the working range of the magnet.

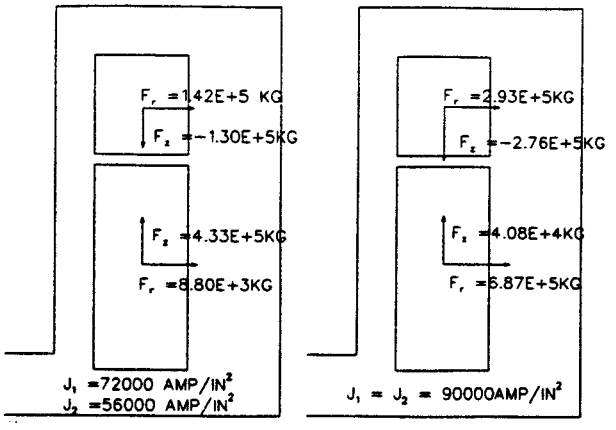

Fig. 3. Integrated total axial and radial forces on inner and outer coils for two critical cases.

addition to magnetic loads. The STANSOL results should be viewed relative to the goal of keeping the coil in radial compression at all points since a composite coil is weak relative to radial tension at low temperature. Also it is desirable to have a moderate hoop stress (<20000 psi) because the critical current depends on the hoop stress (in addition to the usual dependence on current density, on the transverse magnetic field, and on temperature). Another bad feature of a large hoop stress is that cyclic strain can degrade the Cu matrix through fatigue because yield strength of Cu is around 13000psi.

4. Coil Winding Method

We have considered several options for winding the coil, however, they may be broadly categorized as two, which we call 'free coil' and 'tightly banded coil'. For the tightly banded coil two dimensional stress distributions have been simulated using the program written by John DeKamp[3], but results are not included in this report, because we still do not have good understanding of several puzzling aspects of the axial force results. For the tightly banded case, using the Poisson and the STANSOL program for the radial force, we estimate that the friction coefficient between coil and bobbin would need to be nearly 1 in order for the radial clamping force to prevent axial slipping, even if 20000psi winding and 30000psi 1 inch aluminum banding is used. This then means we need even larger winding and banding preload which is not attractive because the resulting hoop stress values exceed prudent design limits.

The free coil system has an intrinsic advantage in that the coil moves with the stress to give a stress relaxation effect. Three free coil versions have been considered and calculated. One of these uses stainless steel for the bore tube and tensioned aluminum as the banding. In this case very weak winding preloads are used so that a very small magnetic force will lift the coil free of the bore tube (J1= J2 =4500Amp/cm^2, 3.7 Tesla at midplane), (Fig. 4), thereby avoiding frictional heat at high fields where the thermal margin is tight. The coil can withstand the sudden movement at the lift-off point without quenching provided the thermal energy at the moment of detachment

doesn't raise the coil temperature to more than 10K. Calculation showed that thermal energy is slightly less than the enthalpy difference of conductor between 4.4K and 10K, but this is borderline when thermal nonuniformities are considered. The calculation however assumes

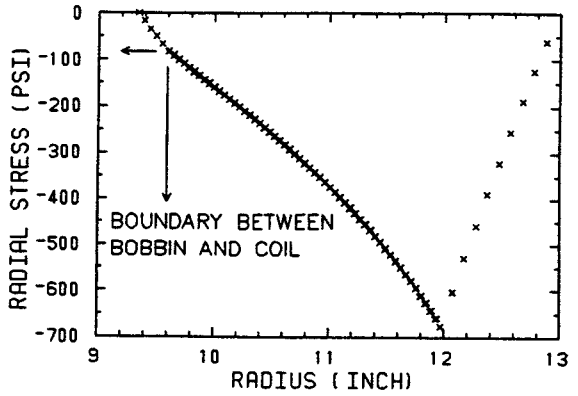

Fig. 4. Radial stress after cooling and before energizing the coil. Winding tension 630 psi in the conductor and 500psi in the aluminum banding.

lift-off to occur at the F_r=0 point whereas the coil movement is most likely to occur in a series of steps near this point. Dividing the heat energy into steps is more favorable, but it is never-the-less difficult to be completely sure that the coil will not quench.

Another choice for winding is to use an aluminum bore tube and stainless steel with a 20000psi winding tension as a banding. In this design the coil becomes completely free just after cooling down as shown in Fig. 5, since the aluminum has a bigger thermal contraction than copper or stainless steel. There is then in this case no concern as to a quench at the moment of detachment as in the previous case, since the field is off at the point where lift-off occurs. Unfortunately, an aluminum bore tube is expected to be difficult to weld, and the coil might be burned during welding due to the high thermal conductivity of aluminum.

At this time the third free-coil choice is thought to have the most attractive features.

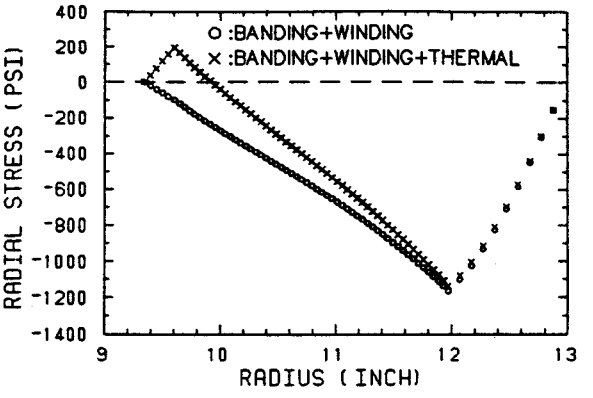

Fig. 5. Radial stress before and after cooling the coil. Winding tension 630psi in the conductor and 20000psi in the stainless steel banding.

This option uses a bimetal (Al+S.S.) bore tube and stainless steel as a banding, but, bimetal will be fabricated as a composite rather than purchased. Coil will be almost free from bobbin after cooling down like the aluminum bobbin case, but welds will attach to the stainless steel and so will not be a problem. The radial stress will be lower, but it was difficult to use the code to calculate the residual radial tension. A simple hand calculation told us that a part of winding and banding tension effects can be left even though they are small enough (<50 psi) to consider the coil effectively free from the bimetal bobbin.

In the future we will work to get a clear understanding of the two dimensional program so we can get more realistic pictures of the stress distributions in the coil.

References

1. M.T. Menzel, H.K. Stokes Poisson/Superfish Group of Codes, Los Alamos Nat'l Lab (1987).
2. W.H. Gray, D.L. Levine, Oak Ridge National Lab (1976).
3. T. Antaya, et al, Magnetic Structure for a Superconducting Variable Frequency Electron Cyclotron Resonance Ion Source, IEEE Trans. Mag 25:1671(1989).

PROGRESS ON THE MEDICAL CYCLOTRON

H. Blosser, J. Bailey, E. Kashy, F. Marti, R. Morin, R. Ronningen, J. Vincent, J. Wagner, G. Zheng (NSCL); E. Blosser, G. Blosser, R. Maughan, W. Powers (Harper-Grace Hospitals)

The report on the cancer therapy cyclotron project in the 1988 Annual Report was written in October 1989 and gave the status of the project as of that date. In this article, written in July 1990, we comment briefly on developments since October 1989 and refer the reader to the previous report for a more complete description of the cyclotron project. (1988 NSCL Annual Report, p. 167).

As noted in the previous report, a K100 superconducting cyclotron for medical therapy had been constructed and brought into operation at NSCL. Fig. 1 shows a schematic view of the cyclotron on its rotating gantry and Fig. 2 is a photograph of the therapy unit assembled for test runs at NSCL. The goal of the medical cyclotron project is to provide neutron beams for treatment of cancer in a physical setting matching that of top quality electron linear accelerators so that the presumed beneficial effects of the high linear energy transfer (LET) characteristic of neutron radiation can be evaluated in a setting which is otherwise comparable to the low LET treatments from electron linacs and cobalt units. In June 1990 testing of the medical cyclotron at NSCL was completed and on July 10, 1990 the cyclotron was moved to Detroit and installed in the Gershenson Radiation Oncology Center of Harper Hospital where it will be a central element of a comprehensive radiation therapy system for cancer. Financial support for the project has been provided by Harper-Grace Hospitals, Inc.

The cancer therapy cyclotron uses a high field superconducting magnet to achieve a K value of approximately 100 MeV in a structure which weighs less than 25 tons. The reduction in weight is approximately 10 fold relative to a typical room temperature cyclotron of the same energy. The reduced weight allows the entire cyclotron to be mounted directly on a rotating gantry so that neutrons produced in an internal

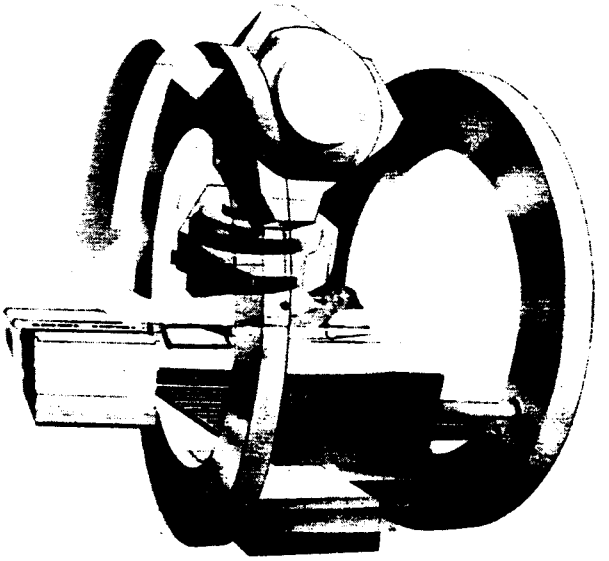

Fig. 1 Schematic view of the superconducting medical cyclotron and gantry system. The gantry consists of two large rings which can move the cyclotron to any desired azimuthal location relative to the patient (two locations are shown in the drawing).

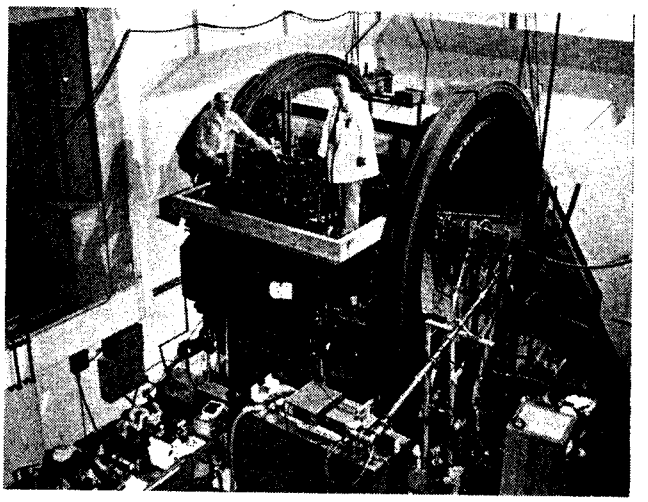

Fig. 2 Photo of the superconducting medical cyclotron on its gantry. Dr. William Powers and Dr. Henry Blosser are standing on the cyclotron.

target can be directed at a supine patient from any azimuthal direction, i.e., from above, below, left or right of the patient. With such an arrangement a strong dose peak in the region of a tumor can be obtained in spite of the overall exponential attenuation of the neutrons in tissue (half value depth ~13cm). As an example, the effect of superimposing three beams entering from respective 120° directions is shown in Fig. 3, which gives isodose contours from a treatment planning computation; the dose to the tumor is substantially higher than the dose in any of the entry regions, and the dose peak in the tumor could be further accentuated by superimposing a larger number of beams in situations where it would be medically important to provide a still stronger dose peak relative to the normal tissue dose.

As indicated in the previous annual report, the medical cyclotron reached full design intensity for the first time in October 1989. (The sentence in the last paragraph on page 167 should read: "Beam tests in the hospital cyclotron began in the Spring of 1989...") In the period from October 89 through June 1990, the cyclotron was operated extensively to establish its overall reliability and to test modifications to a number of components made for the purpose of increasing reliability. In these tests one important problem was uncovered,

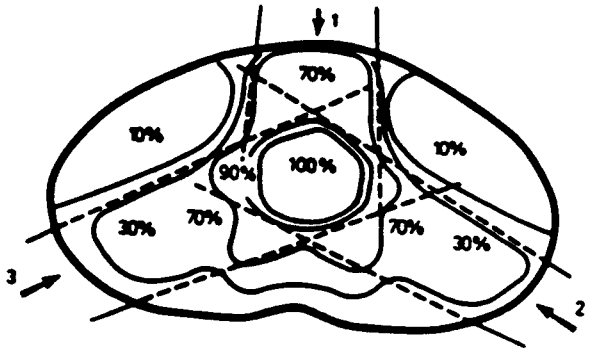

Fig. 3 Computed isodose contours for a three-field treatment for cancer of the bladder.

namely that the superconducting coil quenched on an infrequent but troubling number of occasions and with some indication that the rate at which the quenches were occurring was increasing, two such quenches occurring in 1989, two each in the months of January, February and March of 1990, five in April 1990, one in May, and none in June. One of the quenches occurred after the magnet had been operating in a steady state condition for more than an hour; the remainder were all just at the end of a turn-on ramp.

The quench process is difficult to study because it is rare and nonrepeatable; also several deliberate efforts to induce quenches by subjecting the coil to extra stresses have not caused quenches. As examples, the hypothesis that the quenches are due to conductor movement was checked by increasing the coil current 2 amps above the normal operating value (giving a 3.5% increase in the force on the conductors) -- this did not cause a quench; the hypothesis that the quenches are due to heat produced by eddy currents generated in the magnet turn-on cycle was checked by using a ramp four times faster than normal in the region approaching the operating point -- this likewise did not produce a quench; the hypothesis that the quenches are caused by a reduction of lead gas cooling flow due to blockages developing or opening in parallel helium passages was checked by deliberately opening and closing valves in alternate cooling passages and by installing a continuous monitor on the voltage drop in the leads; the valve openings and closings did not induce a quench and the lead voltage monitor showed "normal" voltage behavior at the time of each of the last 16 quenches.

A weak quench correlation can be identified relative to the temperature of the magnet prior to starting the helium fill and the time delay between completion of the fill and the start of the turn-on ramp. An operating policy of waiting for one hour between completing the fill

and starting the ramp was introduced in early March and appeared to eliminate quenches until the runs in early April when quenches occurred even when the one hour wait rule had been followed; the April runs also included a quench in the circumstance where the magnet had been in steady state operation for more than one hour. Thus far no quenches have been associated with rotation of the cyclotron or with beam on, but this could be statistical since the fractional time which the magnet has been operated in the rotated condition, or with beam on, is small compared to total hours of operation.

At present two avenues of attack on the quench problem are in process. One is to construct a replacement coil and the second is to lower the cyclotron energy by a few percent to reduce the overall magnetic load on the coil (which increases the operating margin relative to thermal fluctuations). To open the way to shift to lower energy operation if desired, a series of magnet maps were made in late May covering the operating range from 45 to 48.5 MeV. With this data and with results of a shimming development study in which a set of shims appropriate for improving the isochronism of the full energy operating point were designed and measured, we are positioned to easily implement a shift to lower energy operation if that is at any point desired.

The option of building a back-up coil involves sizable expenditures and will require six to nine months to complete the work, but would give a coil free of two important errors which are likely candidates as significant causal factors in the quench problem. One of these errors in the original coil involves inadequate preload in the winding pack because the elastic properties of the formvar insulation were incorrectly estimated in design calculations. This error was later offset by inserting a "shrink fit" stretcher ring in the bore of the coil, but this is less effective than a more proper solution of winding the coil with higher tension and of adding an outside layer of winding reinforcement ("banding"). The second error in the previous coil involves the inadvertent use of ordinary copper rather than high purity copper in connecting bolts which join the coil superconductor to the external leads superconductor. As a consequence of this error, the coil's vapor-cooled electrical leads require much higher gas flow than is normal at their current rating and, if the lead gas flow is abruptly interrupted, a quench occurs in 11 seconds. In a second coil this joint would be handled in a much more careful way.

Other cyclotron operating problems which have been uncovered in the test runs are relatively minor in comparison with the coil quench issue. Improvement projects include efforts to speed the response of the control system, efforts to improve the regulation of the rf voltage, and a number of mechanical improvements to increase the operating life of the ion source and of various electrical contacts in the rf system. These efforts have already led to significant improvements in the problem areas observed and, with the exception of the quench problem, have brought performance to medically acceptable standards.

Operation of the cyclotron at the Hospital is expected to begin in August 1990. Biological intercomparisons with other neutron therapy facilities and dose distribution studies are expected to require approximately six months and patient treatments will begin when these studies are complete.

CENTRAL REGION STUDIES FOR THE HARPER HOSPITAL CYCLOTRON

J. Bailey, F. Marti and H. Blosser

The medical cyclotron central region has been reduced in size from the design previously reported in order to allow operation with lower accelerating voltages than were contemplated in the original design. Changes were also made in the source position and slit shape to obtain higher beam currents.

Orbit studies of the original central region electrodes showed that the initial time acceptance window was fixed by the central region posts, which define the accelerating gaps. Vertical focussing was good for any orbit that cleared these posts. The design calculations also indicated that the width of the time acceptance window decreased, as the operating voltage was decreased, with a cutoff slightly below 36 kV. The goal of the study described in this report was to develop a central region configuration which would allow operation at still lower voltage.

An approximation to the needed electrode configuration was obtained by scaling of the previous geometry. In general, to make a scale change in an orbit determined by a Lorentz force, it is necessary to similarly scale the geometry of the electromagnetic fields, and the magnitude of the electric field, with the magnitude of the magnetic field remaining unchanged. This scaling of both the geometry and the magnitude of the electric field corresponds to scaling the geometry of the electric potential while scaling its magnitude twice. Thus, to achieve scaled orbits (similar in timing, centering, and focussing) a uniform scaling of the geometry of a central region allows the accelerating potential to be scaled by the square of the geometric scaling factor.

The new, reduced voltage central region, is based on a scaled reduction of the previous central region, but with a number of exceptions which break the conditions required for complete geometric correspondence of the families of orbits. A first such deviation is that the geometry of the magnetic field is left unchanged; this deviation from true scaling is however not important, since the magnetic field is nearly constant at the center of a cyclotron. Scaling of the electrodes was also limited to the region within 1 inch of the central axis in order for the electrode spiral to match smoothly onto the existing dees and also, for mechanical reasons, vertical dimensions of the electrodes were left unchanged. The horizontal scaling factor was chosen to be .93 leading to the electrode configuration shown in Fig. 1, and corresponding to an expected 14% reduction in the needed accelerating voltage. Another deviation from complete scaling involved the diameter of the source chimney which was kept at .25 in, so that the same source could be used. This was an important scaling deviation since it reduced the important source to puller gap by more than the scaling amount. Since many aspects of the new central electrodes did not follow scaling laws, it was necessary to integrate orbits to determine the behavior of the new system.

Computer calculations of orbits in the reduced geometry indicated that the time acceptance window was largely unchanged, but the phase of the orbits relative to the rf voltage was shifted by 8 or 9 degrees at the 1 in. boundary in the direction to weaken the electric focusing and as a consequence, orbits at the later starting times are lost vertically as illustrated in Fig. 2, and the range of useful starting times is then actually somewhat restricted relative to the original central region. The better match between the voltage assumed in the calculations and the voltage

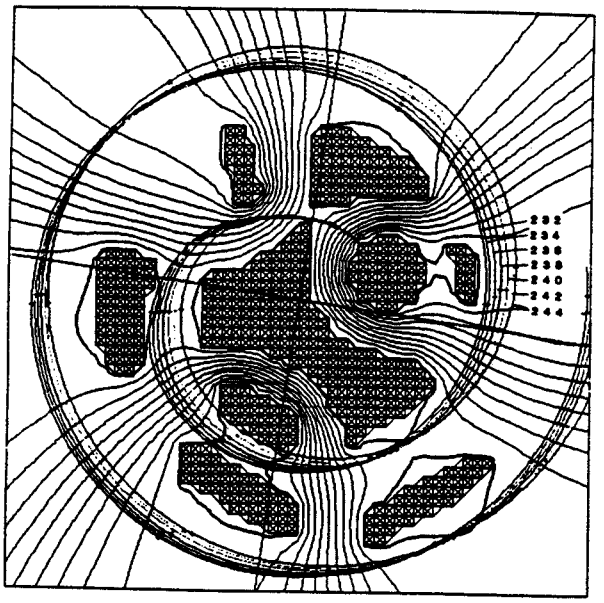

Fig. 1: Equi-voltage contours in the new, low-voltage central region electrode system for the Harper Hospital cyclotron. The grid is 1.86 in. by 1.86 in. -- the magnetic coordinate system is indicated by the slightly rotated cross with θ = 0 at the right. Equi-potential lines from 0% to 100% in 10% steps are shown along with a set of typical midplane "central-ray" orbits. Numerical labels at the right give the phase of the rf voltage at the time the computation started where 0 and 180 are the times at which the voltage changes sign. Small crosses on each orbit mark the particle location at successive voltage reversal points. (Some of the orbits hit or pass too close to electrodes leading to small discontinuities as can be seen weakly in some of the cross locations.) For these runs the ion source is at its "standard" position (not the "forward" position discussed later) and trajectories close to the source are from the analytical cylindrical electric field solution as described in the text. Amplitude of the rf voltage is 38 kV.

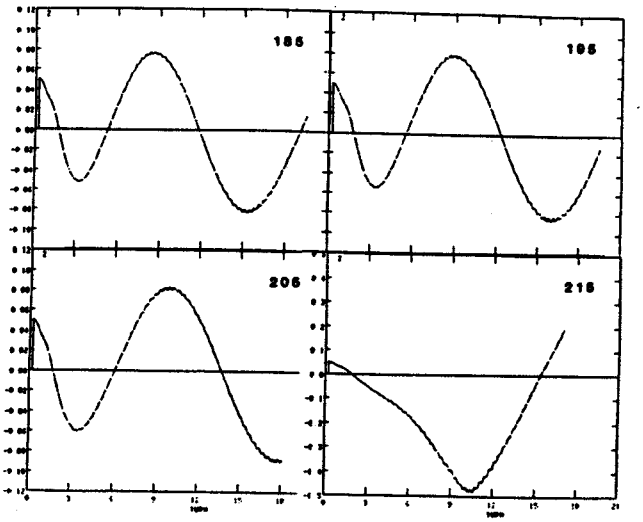

Fig. 2: Vertical motion in the reduced field for V0 = 33 kV and RF starting times tau = 185, 195, 205, + 215. Note the different scale for tau = 215. This orbit hits the dee on the 9th turn.

which is actually achievable in the cyclotron should however more than offset the reduced time acceptance because of improved radial transmission through the slits.

Central region electrodes corresponding to the new geometry were machined and installed and the cyclotron produced its first accelerated beam. Initially, however, the beam current was some two orders of magnitude lower than the design specification of 10 microAmps.

A search for the cause of this low beam intensity, eliminated the area outside of the central region, and demonstrated that it could not be attributed to a poor vacuum. A large mark, found on the inside of the puller, narrowed the search to the source to puller region.

Since the cyclotron operates on third harmonic in a 4.6 Tesla magnetic field, the sensitivity of the source to puller gap is greatly enhanced. An rf half cycle is only 4.8 nanoseconds, and on this scale particles take a long time to cross the source-to-puller accelerating gap. Insufficient or incorrect detail in this part of the calculation can easily lead to quite misleading orbit results.

At this point all orbit calculations (including the studies thus far described herein) had assumed that the equi-potential representing the plasma boundary was located at a radius corresponding to the outer diameter of the ion source chimney. Initial orbits were

assumed to start at the center of the source exit slit on this radius, and were integrated in an electric field obtained from the analytic solution to concentric cylinders, with a constant magnetic field directed along the cylinder axis. At a transition point close to the source, but far from the hole in the puller, and at least two grid points from any fixed electrode potentials in the relaxed potential field, the orbit calculation shifted to the central region orbit code CYCLONE, using the measured magnetic field grid and electric potential grids obtained for the electrode geometry using RELAX3D, a relaxation code developed at TRIUMF.[2]

The low beam current suggested that computational modeling of the source to puller region had important errors. To include finer detail, a new electric potential grid was made of just the source to puller region, so that details of the extraction slit could be specifically included. At this time the extraction slit in use in the source was fabricated by machining a .01 in. deep flat in the .015 in. source wall, and cutting a vertical, .01 in. x .375 in. rectangular slit through the remaining .005 in. wall at the center of this flat. The new relaxation grid included all of these details, and the equipotential representing the plasma boundary was placed at the inner diameter of the source chimney (rather than at the outer diameter as in previous runs.) The electric field discontinuity at the plasma and electrode boundaries leads to unrealistic field values if an interpolation is used which includes grid points inside the plasma or inside an electrode -- to avoid such irregularities, orbit calculations in this field were started at the exit end of the .01 in. wide slit. Even with this unrealistically favorable location, the orbits needed both a high starting energy and a high operating voltage to clear the puller. In the actual cyclotron, such conditions would be expected to produce little to no current (in agreement with the experimental measurements) and showing the need for still greater detail in the source to puller calculations.

New slit designs were then tried using cutters of 120 and 150 degrees to give a knife edged slit, instead of machining the wall flat. The knife edge makes the electric field stronger at the plasma boundary, and provides radial focussing close to the source. For these studies the plasma boundary was again assumed to be at the inner diameter of the source, and the orbits were started .005 in. away from this boundary. The computations showed a slight improvement over the original slit in operational characteristics, but high voltages were still required as indicated in Table I. When these slits were tried in the cyclotron, beam current increased, but not by the orders of magnitude needed.

Table 1: Calculated starting time acceptance windows of the reduced central region and the associated allowed range for the accelerating voltage. Various deuteron starting energies were explored in the calculations as indicated, and various slit configurations were used as indicated in the sub-headings and as described in more detail in the text. Some of the runs also included a rotation of the source, which shifts the angular location of the output slit relative to the puller.

Slit Type	Dee Potential (kV)	Starting Energy (eV)	RF Window (deg.)	Rotation
120 degree knife edge, original position.				
	38-40	10	185	
	36-38	100	185	
	39	20	185-205	
	39	20	185-200	CW 6 deg.
150 degree knife edge, original position.				
	39	20	185-208	
	39	20	185-205	CW 3 deg.
Rectangle, .035 in. forward.				
	30	20	---	
	34	20	212-222	
	38	20	231-238	
	38	20	230-240	CCW 10 deg.
	38	20	---	CW 10 deg.
Hole, .035 in. forward.				
	30	0	---	
	34	0	205-220	
	38	0	232-244	
Hole, original position.				
	38	0	---	

Next the .01 in. wide, rectangular slit was moved .035 in. closer to the puller. This decreased the gap to .1 in., increasing the peak electric field from 100 kV/cm to 135 kV/cm, and decreasing the transit time. In the computer simulation this forward displacement provided current at lower accelerating voltages than previous slits. In the cyclotron the rf system operated reliably in spite of the increased electric field and the beam current increased by an order of magnitude.

In the course of experimental testing, one of the .01 in. wide slit chimneys proved to be too long, and buckled after the plasma heated it. This buckling opened a small hole in the slit, eventually causing the rf to fail, but not before obtaining currents of 5 times the design value. At this point an additional vacuum pump was installed on the cyclotron which allowed running the rf with larger area output slits in the source (previous efforts to use larger slit areas to increase the beam current had been unsuccessful due to source gas degrading the vacuum and producing a multi-pactoring glow discharge which prevented high power operation of the rf). Noting the good performance of the rather circular hole which had developed in the buckled source, a chimney was fabricated with an .06 in., 60 degree knife edge hole. This source, when run in the same forward position as the rectangular slit, provided the design beam current, with a well defined beam spot.

Computer simulations of an .08 in. hole, with a 120 degree knife edge were then run with the source in the close-to-the-puller position as shown in Fig. 3. This time the potentials inside the plasma and electrode regions were adjusted so that the electric field inferred from interpolation and differentiation in the numerical grid would be continuous and smooth at all points outside the plasma surface. With this field, realistic orbit computations could begin at the plasma boundary and the initial energy could scan the 0-100 ev range expected

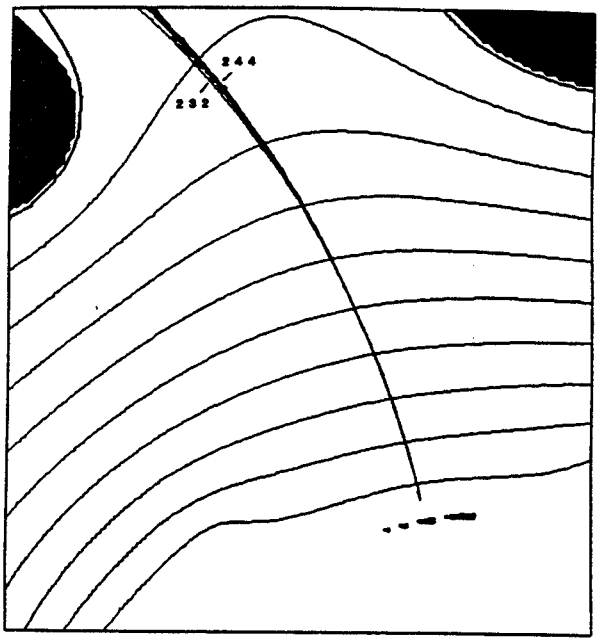

Fig. 3: Equi-voltage contours for the very detailed source-to-puller computations. The ion source has an 80 mil diameter exit hole with a 120° knife edge. The source is in the forward position, and the figure covers a .1625 in. by .1775 in. area. Starting times and voltage contours are the same as in Figure 1, and the rf voltage amplitude is 38kV.

for particles leaving the plasma. These simulations showed wider time acceptance windows than did the rectangular slit when run in the forward position. The increase in acceptance time was, however, far short of the amount which would nominally be needed to account for the order of magnitude increase in the measured beam. The increased current from the "hole" is then thought to be related to an enhanced emission effectiveness associated with the large slit area at the midplane, but the effect of starting at different locations in each slit was not studied. In the simulation, when the slit with the hole was moved to the original position, the beam failed to clear the electrodes, even at high voltages.

The process of extending the potentials into the region inside the plasma is also arbitrary in considerable degree. To simplify, we assumed that the plasma boundary was a fixed conducting surface. We then made the assumption

that the shape of the plasma surface is the same as the inner diameter of the chimney. Next this cylindrical surface is approximated by fixing potentials on a rectangular grid and RELAX3D is used to obtain potentials at the grid points away from the fixed boundary-value potentials of the points representing the surfaces of the electrodes and plasma. The electrode surface grid points and the process of adjusting potentials needs to shift these points in accord with their displacement from the true cylindrical surface and all of this should lead to a field which satisfies Poisson's equation. The detailed corrections are then arbitrary to a sizable degree and based largely on giving a field which will be smooth, continuous and slowly varying as a function of displacement from the true cylindrical surface. Even though arbitrary, this process has the virtue of being free of certain identifiable errors associated with the previous approximations (using a starting location displaced forward from the plasma, etc.).

Experimentally, the improved vacuum pumping made it easy to quickly test a variety of source slits. Various "hole type" chimneys were then tested and the final configuration uses a hole of approximately .06 in. diameter with a 120° knife-edge and beams of up to 60 microamps are readily obtained at voltages of approximately 33kV. Perhaps most importantly, the experiments have demonstrated that cyclotrons can operate effectively with very small source to puller gaps corresponding to electric fields in the vicinity of 130 kV/cm.

References

1. J. Griffin et al., MSU Annual Report (1985), p. 192.
2. C. Kost, TRIUMF, U.B.C. Canada.

MEDICAL CYCLOTRON CONTROL SYSTEM

G. Zheng, R. Morin, J. Vincent, J. Brandon, H. Blosser

Introduction

The K100 Medical Cyclotron, constructed for Harper-Grace Hospitals, will be used for neutron therapy in their Gershenson Radiation Oncology Center.[1] To produce the required neutrons the K100 will accelerate a deuteron beam onto an internal beryllium target at a fixed energy of 50MeV. Compared to a normal research cyclotron, the K100 cyclotron has many simplifying features: its rf frequency is fixed at 105MHz, trim coils to shape the magnetic field are not required, beam extraction and beam transport is not needed, etc.[2] All of these contribute to allowing the K100's control system to be comparatively simple.

General Features

The K100 Cyclotron control system consists of a Macintosh Plus Computer, an ACRO-900 Data Acquisition Interface Unit, and the Control Hardware System. The Control Hardware System includes device controllers and interfaces, metering and instrumentation, power supplies and associated equipment. Most electronics are packaged in NIM modules and powered with two NIM bin power supplies. Some electronics are built in standard 19" panel boxes and separately dc powered. The control hardware, including the ACRO-900 system, is mounted together in a single standard relay rack; deviations from this central electronics location are made for those items that have to be located close to the cyclotron (e.g. the trimmer local drive, the "popup target" local controller, etc.).

Figure 1 shows the control system block diagram. The power supplies (transmitter, magnet, ion source, etc.) and devices (trimmer, gas valves etc.) each have their own local controller.

The control system has two local operating modes, "Remote" and "Local". When set to Remote the cyclotron is controlled by an operator using the Macintosh computer as a control console. The computer is connected via a serial digital bus (RS232) to the ACRO-900 system. The ACRO-900 has DAC, ADC and digital I/O which provides a way for the Macintosh to set and measure analog signals and discretes. Operators use the computer screen, keyboard and mouse to control and monitor cyclotron operation. A printer attached to the Macintosh provides the hard copy records needed for monitoring.

When tuning the cyclotron, or for trouble shooting, operators may run equipment locally. In this case the Remote/Local switch on the relevant local controller is set to Local and operators use the front panel switches and potentiometers to control the unit.

The control system's major functions include:

- On/off control of power supplies and devices
- Setting and regulation of parameter values
- Measurement and display of parameter values
- Indication of discrete states
- Interlock and safety protections

Table I summarizes the control requirements for the most important cyclotron parameters. Table II shows the cyclotron measurement parameters. Most parameters are collected by the computer as well as displayed on local panel meters. Those with an asterisk are parameters which are at present only measured locally.

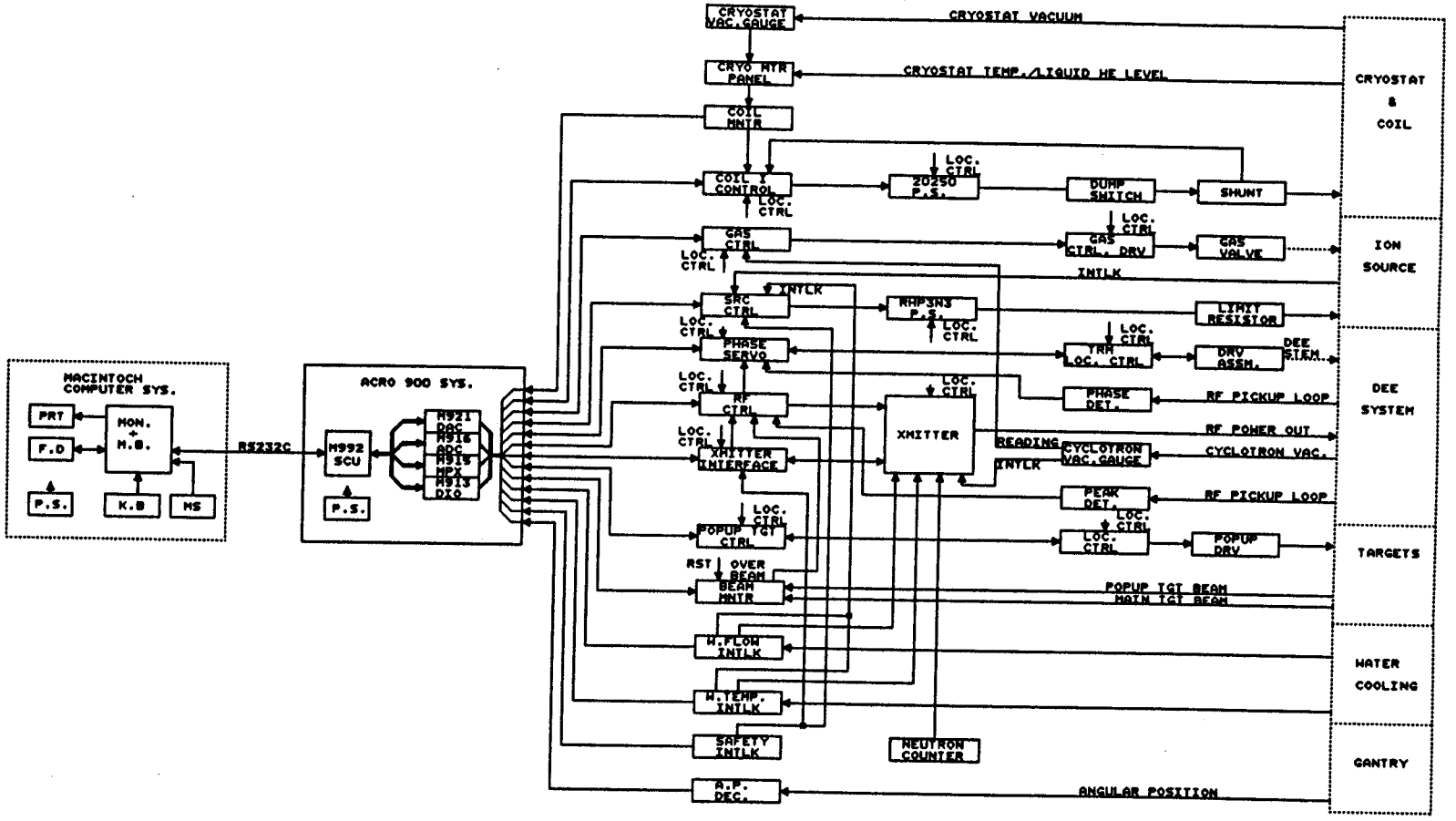

Fig. 1 K100 Cyclotron Control System Block Diagram

Size	Document Number	RE
B		
Date:	July 31, 1990 Sheet	of

Table I. The K100 Cyclotron Major Control Parameters

Magnet Coil Current Control:	
- Normal Operating Current:	202.13 A
- Current Regulation:	2.5e-5
- Variable Current Range:	180 - 230 A
- Current Setting Resolution:	0.01 A
rf Control:	
- rf Frequency:	105 MHz,+/- 10 KHz
- rf Power:	25kW
- Dee Voltage Control:	0 - 35 KV,+/- 0.01
Ion Source Control:	
- Arc Voltage:	0 - 3 KV
- Arc Current:	0 - 1000 mA
- Current Setting Resolution:	30 mA
- Gas Flow:	0 - 5 cc/m,

Macintosh Computer and Control Software

In addition to the major functions mentioned previously remote capability is provided to:

- Detect and latch malfunctions and initiate protective action
- Detect and issue alerts for out-of-limit or inconsistent conditions
- Guide manual control sequencing of devices
- Log and print parameter values
- Report control system health and status

Following standard Macintosh user interface methods the user has access to a variety of functional display screens by making choices from a main menu bar that reveals pull-down menus when activated with a mouse controlled cursor. Figure 2 shows one of the screens (Control Page) and the main menu bar that is always available. Each of the main menu categories has several associated sub-functions that can be selected, each with its own display format. In this way, a total of seventeen display screens or pages are available; the most important are summarized below.

- Control page for normal cyclotron operation
- Interlock pages for viewing, resetting and bypassing interlocks
- Operational Values page for specifying default parameter set points
- Parameter Limits page for specifying thresholds and windows
- Operational Log page for printing recorded parameter values

Three methods are provided to set control values via the computer:

- Direct type-in of setting values with the keyboard to change the reference point of servo-controlled devices
- Adding up or down increments to the present servo reference setting by clicking the mouse on an increment or decrement button
- A drive command to move motor driven non-servo controlled devices "up" or "down" from their present setting, achieved by holding the mouse button down with the cursor positioned over the appropriate arrow on the screen

For the servo controlled devices, the computer sends a reference voltage via the ACRO-900 DAC to device or power supply controllers.

Table II. Parameters Measured by the the K100 Cyclotron Control System

Cryostat and Coil System:
- Coil Current
- Coil Voltage
- *Coil Lead Drop
- *Helium Gas Pressure
- Liquid Helium Level
- Cryostat Vacuum
- *Cryostat Temperature
Ion Source and Gas Flow System:
- Source Voltage
- Source Current
- Gas Flow
rf System:
- Transmitter PA Plate Voltage
- rf Phase Trimmer Position
- Dee rf Voltage
- *rf Forward Power
- rf Reflected Power
- Cyclotron Vacuum
Beam and Others
- Main Target Beam Current
- Popup Target Beam Current
- Gantry Angular Position
* = local readout only

For motor drives the computer controls relays using the ACRO-900 digital outputs to simulate the center off, up and down momentary switches implemented for local control.

Control of power supplies, valves, and device states is another function of the control computer. Currently, with one exception, the "on" or activated state of a power supply can only be commanded manually. A provision has been made for automatic sequencing in which all power supplies would respond to a single master "turn cyclotron on" command but this capability has not yet been implemented; the one automatic turn-on process in use at present recycles the rf system plate voltage when it has been turned off by an interlock following a dee spark. Power supplies or device states are turned off automatically whenever pre-programmed conditions indicate that this is the appropriate action. The desired device state is communicated to the device controller using discretes set to appropriate logic levels.

As Table II indicates, fourteen parameter values are measured by the computer. Each parameter is sampled once per second with the exception of rf voltage and beam currents which are measured twice per second. Discrete states are sensed and used to provide advisory or status information, enable or prohibit operational sequencing and to indicate interlock conditions. When malfunction conditions are detected: 1) the operator is alerted to the condition by a message and a repeating audio tone, 2) the interlock is latched to permit detection of transient conditions, and 3) protective actions such as turning off power supplies are taken. In order to reverse the protective action either the interlock must be bypassed or the malfunction cleared and the interlock reset. For test purposes, individual interlocks or groups of interlocks can be bypassed using an authorization code word. If a malfunction interlock is bypassed the operator is notified if the interlock occurs and controls

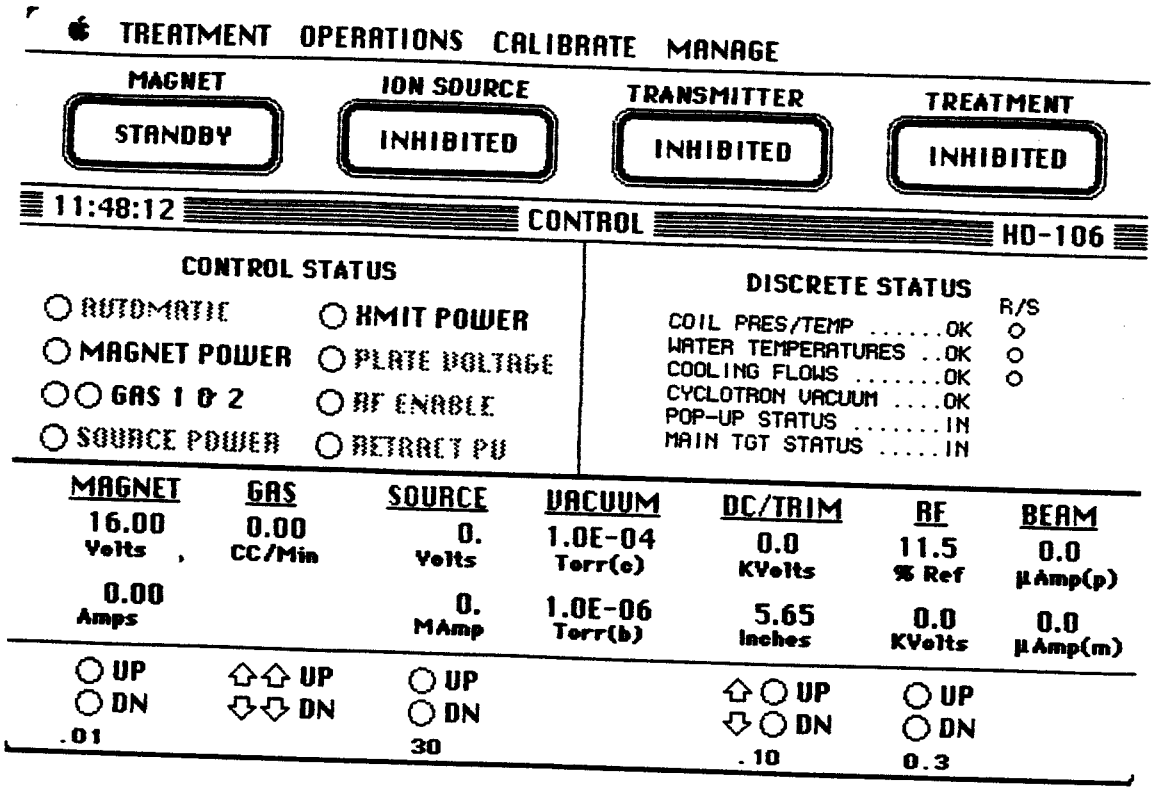

Fig. 2 Control Page Display

are latched until the interlock is acknowledged but the protective action is not taken.

Main Control Program

Figure 3 is a flow diagram of the main program loop. When the program is initially started defaults are established for many variables in preparation for establishing a disk resident status file. If a status file is available it is used, if not a default file is created. The status file permits maintaining operating values, limit settings, interlock bypass states and similar information through a program shut down.

After completing these initialization procedures the main loop of the program begins. Execution is nominally synchronized to a one second cycle. If operator interactions result in the loop taking more than one second the loop starts over as quickly as possible and re-synchronizes to the one second interval in subsequent cycles.

The program loop is very simple and consists of four interactions with the ACRO-900 interface, processing of input data, and updating the display screen. If printer output is enabled this takes place during the data processing block. Except for a few short intervals (when they are placed in a que), real time interrupts handle user interactions with the menu, buttons, edit fields, and other active mouse click screen areas. These items thus receive immediate attention and when necessary the appropriate commands are relayed without delay to the ACRO-900 for device control.

ACRO-900 System

The ACRO-900 is a commercially available data aquisition system. Its System Control Unit (SCU) ACRO-992 has a command and data management program stored in EPROM. The SCU receives commands from the host computer (the Macintosh

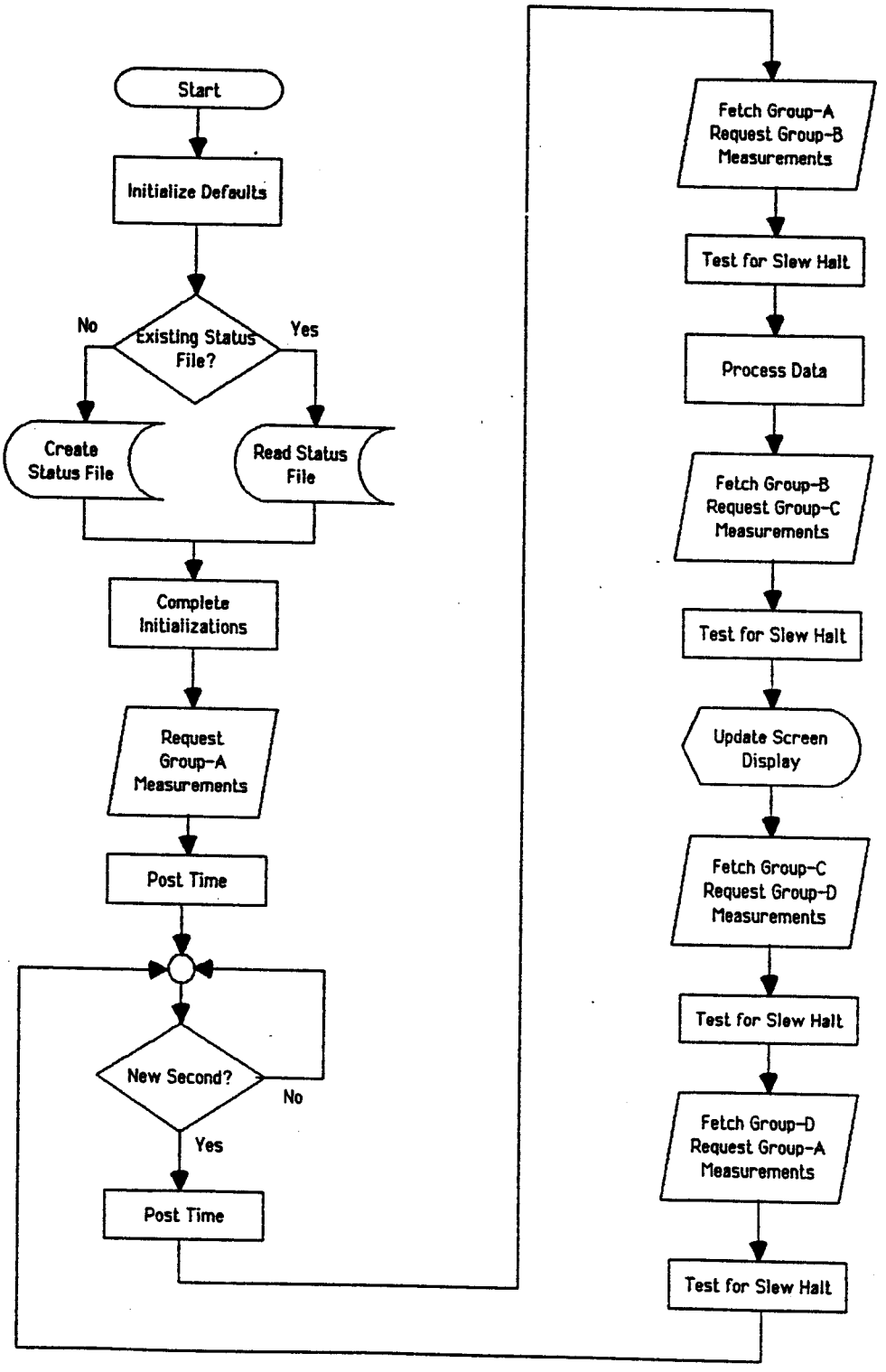

Fig. 3 Main Program Loop Flow Diagram

in this application), translates the commands into the intended measurement or control action, and then passes them to the respective modules for execution. The system configuration depends on the application. The set up for the K100 cyclotron control system is given in Table III.

Table III. ACRO-900 Configuration for the Harper Cyclotron.

ACRO-992 System Control Unit:

CPU:	intel 8088.
CPU Word Size:	16 bits
Processing Rate:	5 MHz
Computer Interface:	RS232
RS232 Baud Rate:	9600

ACRO-921 Analog Voltage Output Module:

Analog Outputs:	8 channels,+/- 10V.
D/A Resolution:	12 bits.
DAC Update Rate:	5 KHz.
Digital I/O:	8/8 channels,TTL.

ACRO-916 Analog Voltage Input Module:

Analog Inputs:	8 channels,+/- 200mV,2V,20V.
A/D Resolution:	12 bits.
ADC Conversion Time:	50 us.
Digital I/O:	8/8 channels,TTL.

ACRO-913 Digital I/O Module:

Digital I/O:	60 independent bidirectional,TTL.

ACRO-915 Multiplexor Module:

Configuration:	8 blocks of 4 relay switches.
Maximum Settling Time:	1 msec.

ACRO-901 Power Supply Module:

Control Hardware

The Control Hardware is divided into six sub-systems (indicated in Fig. 1 by the dotted boxes on the right), namely: 1) Cryostat & Coil Control, 2) Ion Source Control, 3) Dee System Control, 4) Target Control, 5) Water Cooling System Control, and 6) Gantry Control. Each system is designed to carry out a group of specific control tasks as discussed below.

1. Cryostat & Coil Control

The K100 cyclotron magnet coil is powered by a 20V/250A PWM DC P.S. from Power Ten Inc. The specified current regulation of this power supply is 1e-3; an external loop is used to improve the regulation to 2.5e-5. Details of this external loop are shown in Fig. 4. To sense the current, a 0.0004 ohm shunt is connected in series with the coil. The V_{shunt} signal (0 to 100mV for 0 to 250A) is fed back to the current controller to compare with the current setting value (V_{ref}) at the summing point. The error signal provides an input to the 20V/250A P.S. to make its output change appropriately. The load (superconducting coil inductance, room temperature feeding cable resistance, and "dump resistor" resistance) is treated as a first order system. To eliminate the static error and increase loop margin, traditional PI compensation has been added.

The V_{ref} is a very stable voltage source controlled by a front panel tuning pot when in the Local mode, or by the computer via the ACRO-900 when in Remote. To get better setting resolution (0.01A), the reference is broken into two parts:

$$I_{set} = I_i + I_d$$

where I_i is a fixed initial current setting, chosen as 180A, and I_d is an adjustable setting with a range of 0 to 30A. These choices permit the 12 bit DAC to provide a resolution of approximately 7.5mA, thus meeting the resolution requirement of 10mA.

Another important magnet parameter is the output Voltage of the power supply, which is

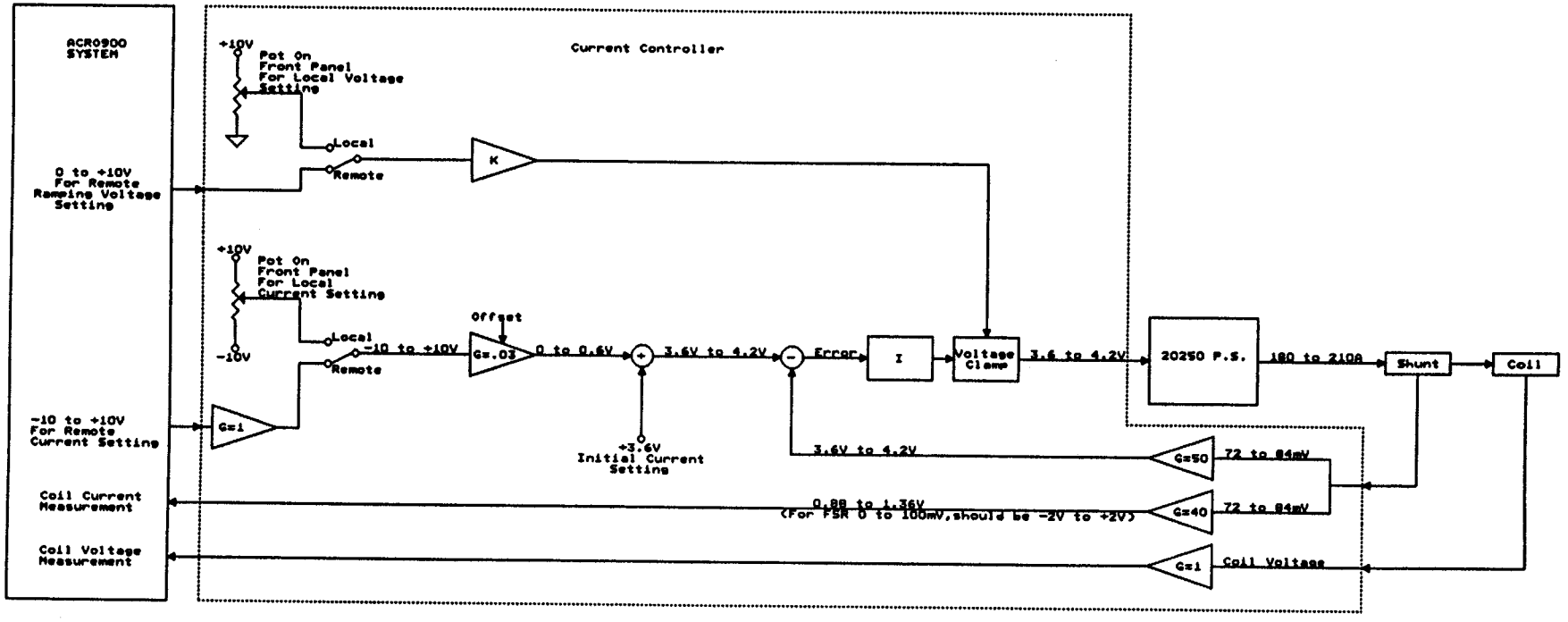

Fig. 4 Coil Current Control Flow Chart

Size	Document Number	RE
B		
Date: April 19, 1990	Sheet	of

programmed by the computer (Remote) or set with a pot (Local). Normally, the full power supply voltage is used as the magnet is first turned on ("starting to ramp") and this voltage is reduced to half when the current exceeds 195 amps and to a low level which gives 0.5 volts at the room temperature lugs of the superconducting coil when the current has settled to the operating point. The 0.5 volts leaves sufficient dynamic range for current adjustment and improves the current regulation compared to higher voltages.

There are three ways to run the power supply, namely, Controller Remote (computer), Controller Local, and P.S. Local. When set to P.S. Local, the external loop and safety interlocks are disabled.

2. Ion Source Control

A block diagram of the Ion Source Control System is given in Fig. 5. The source is powered with a Spellman RHP 3KW P.S., which is a self regulated power supply based upon the Serial Resonant Inverter (SRI) principle and is equipped with remote setting and reading. Reference settings of 0 to 10V for voltage and current give respectively 0 to 3KV for the output voltage maximum and 0 to 1000ma for the output current maximum (and the power supply regulates at the lower of the two maxima). When set to Local mode, operators use two 10*100 dial tuning pots to set the current and voltage.

The gas flow control has two identical channels Gas 1 (usually D_2) and Gas 2 (usually H_2). Each one has an On/Off Valve operated by an electric solenoid and an Open/Close Needle Valve driven by a motor. Control commands from the computer (Remote), Local Panel Switch or Cyclotron Local Control Switch operate the relays, and the relays energize the solenoids or motors to control the gas flow. The flow rate (for gas 1 only)is measured with a Hastings ALL-5 Flow Meter, 0 to 5Vdc corresponding to 0 to 5cc/m.

3. Rf Control

The K100 cyclotron uses a Continental 816R-3 FM Broadcast Transmitter as its rf power source, and a 802A 50W FM Exciter as signal generator and pre-amplifier. The transmitter can operate from 88MHz to 108MHz with 10KHz steps and 500Hz stability; rf output power is 25KW. (The design value of the operating frequency for the K100 is 105.00MHz.)

Software for the rf System Controls is divided into three sub-sections designated as Transmitter Control, Dee rf Voltage Amplitude Control and Phase Trimmer Control. Figure 6 givens a block diagram of the system hardware.

The "Transmitter Control" block includes Filament On/Off, Plate On/Off, Plate Voltage Increment/Decrement, rf On/Off and all interlocks. There are three control modes: Transmitter Local, Control Panel Local, and Remote. When operating in Transmitter Local, control from the computer or the control rack panels is inhibited. When set to Remote the operator can still turn off the transmitter locally for safety reasons. The Panel Local Control is the same as Transmitter Local except that in this mode the interlocks will self latch. The interlocks include transmitter Door Switches, Over Load, Over Voltage, Water Flow, Temperature, Cooling Air Pressure, Cyclotron Vacuum, Neutron Counts, etc. (A full list of interlocks is given in Table IV.)

Voltage on the dees is controlled by the combined effect of the two parameters which fix the transmitter rf power output, namely the Power Amplifier (PA) Plate Voltage and the Exciter Drive Power. The 0 to 10KV plate voltage is set to "manual" control on the transmitter front panel and will normally stay at its maximum of about 9.6KV when running, with lower values available via the "DC up/down" section on the main control page (Fig. 2). With the plate voltage fixed, the rf power is controlled by changing the Exciter Drive

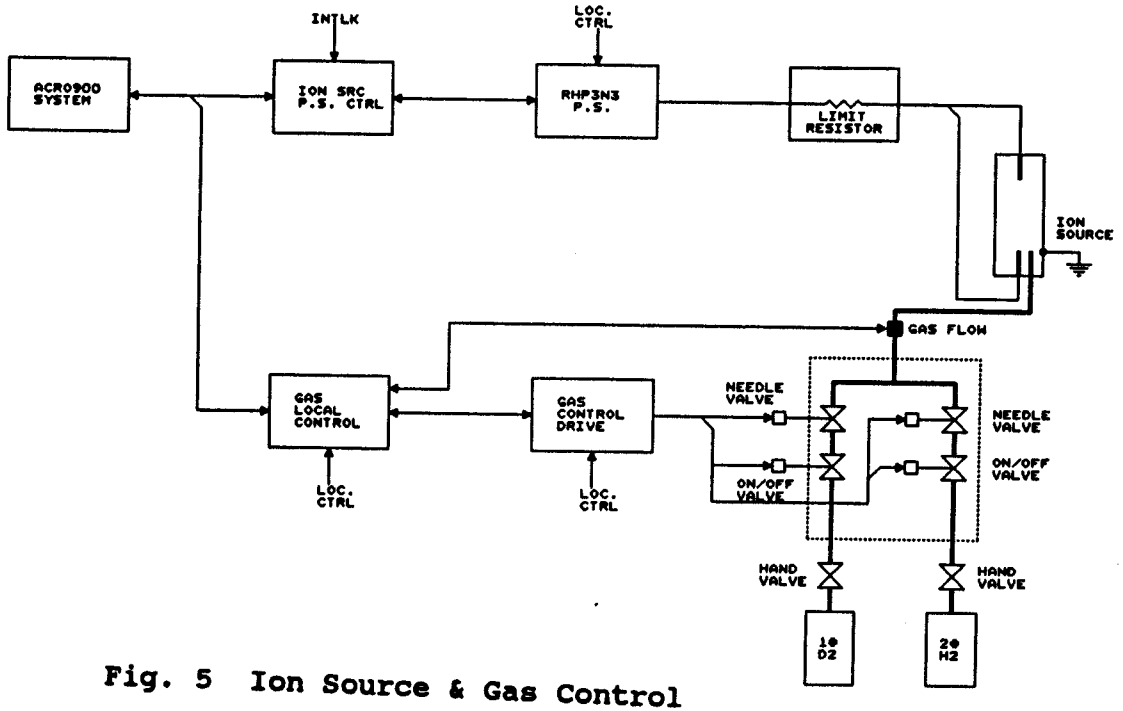

Fig. 5 Ion Source & Gas Control

Size	Document Number	RE
B		
Date:	April 19, 1990 Sheet	of

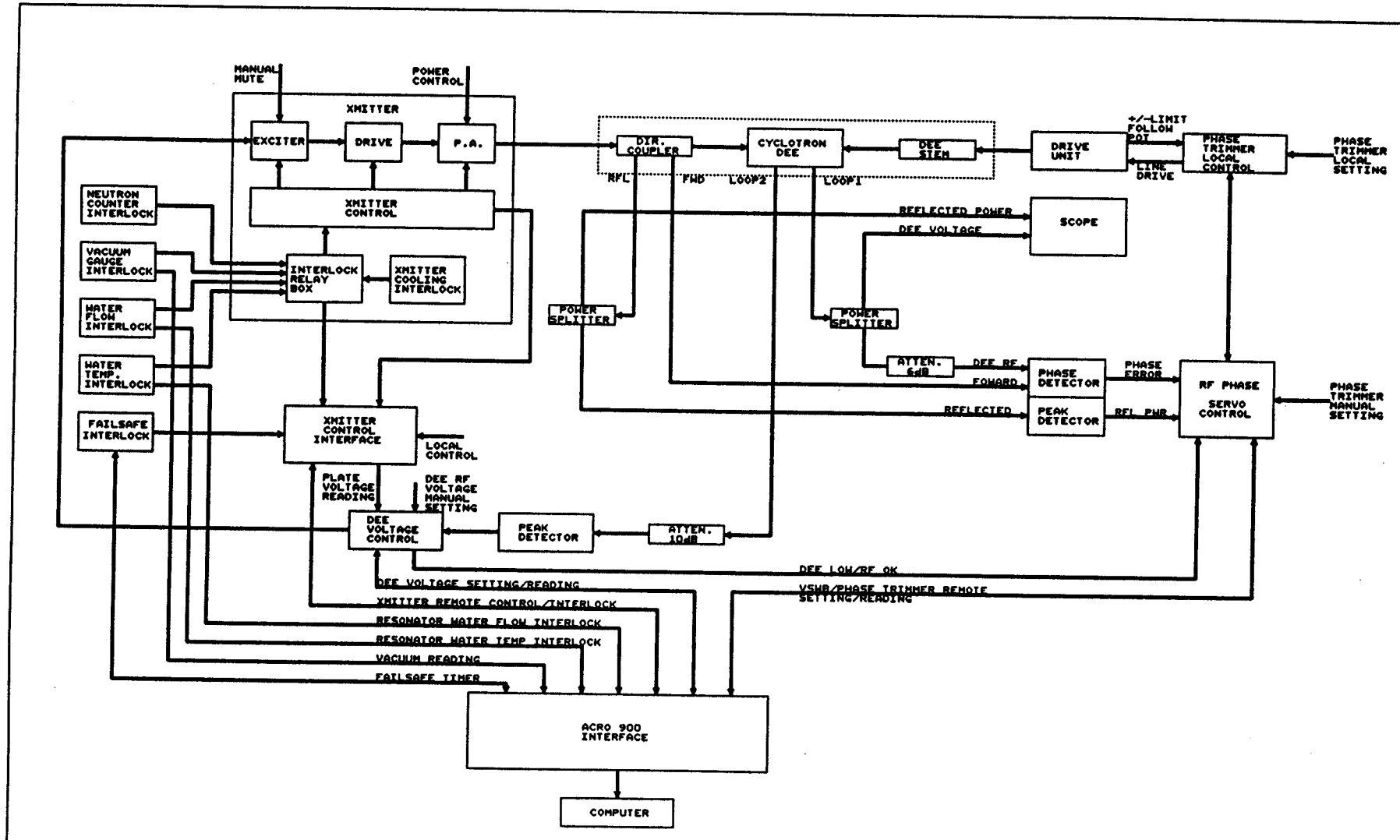

Fig. 6 RF Control System Block Diagram

Size	Document Number	RE
B		
Date: April 19, 1990	Sheet	of

setting. The setting range is 0 to 10Vdc, with a resolution of approximately 0.01V, either from the computer (Remote) or from the Dee Voltage Controller (Local).

A block diagram showing the internal structure of the Dee Voltage Controller is given in Fig. 7. The Dee Voltage is sensed by an inductive loop located in the shorting plane of one of the dee stems and the rf signal from this loop is sent to the rf Peak Detector. The 0 to 10V dc voltage output from the peak detector, representing 0 to 50KV Dee voltage amplitude, is fed back to the controller to compare with the reference setting. The amplified error signal determines the controller output and in turn the exciter drive power to stabilize the Dee voltage at the desired level. The dee voltage controller also includes circuits to turn the rf quickly on at startup, and to turn the rf quickly off if a spark or other malfunction occurs. The action of these elements is discussed later (in the paragraph describing the rf turn-on process).

The "Trimmer Control" automatically tunes the rf resonator to the correct resonant frequency, by activating a motorized drive which changes the position of one of the Dee stem shorting planes (the "Trimmer"). The movable shorting plane is driven by an SS25 synchronous motor via a gear box. When the rf is running with the trimmer module on "auto", the phase error between the rf Forward Power and the Dee rf Voltage is detected by the Phase Detector. This signal is then compared with a window setting in the Phase Servo Module and, if the error is outside the window, the Phase Servo will send a 'Drive Plus' or 'Drive Minus' command to drive the trimmer motor. The shorting plane on the trimmer dee stem then moves to adjust the resonant frequency of the resonator to match the amplifier and thus the transmitter/resonator system is locked at the phase corresponding to maximum power flowing from amplifier to resonator. The Auto tuning feature is inhibited when the dee voltage is lower than the level set by the "dee-low" discriminator.

The rf turn on procedure is as follows: When the transmitter is on and the plate voltage is above a threshold value (which is adjustable from 5V to 10V representing plate voltage 5KV to 10KV), the Dee Voltage Controller initiates a pulsed turn-on cycle, through the circuitry shown at the lower right of Fig. 7. The turn-on pulse is shaped by two parameters, the Step Up setting and the Ramp Up setting as shown in the upper center of Fig. 7 (both settings are 0 to 10V adjustable). The rf drive pulse stays on until terminated by an output trigger from the first event logic loop, the inputs to this loop being the rate of change of the voltage level ("dV/dt") and the level of the voltage ("dee low") on the dee, the latter with a time delay set by the Pulse Width control. After the turn on process breaks through multipactoring and stays on (i.e. exceeds the Dee Low threshold within the pulse width time interval) the pulsing stops and the Amplitude Loop begins to regulate. After a time delay, the rf OK signal will be sent to the Phase Servo and the Phase Loop will start to work (when there is no rf the Phase Loop is disabled so that the trimmer will not run away). If the rf fails to break through multipactoring (Dee Low), or sparks off (dV/dt), the drive is turned off for an interval fixed by the Waiting time control after which the cycle repeats. The Pulse Width and the Waiting Time are adjustable (Pulse Width 0-600 msec, Waiting Time 0-6 sec). Recently a "60 cycle" turn on option (not shown in Fig. 7) has been added to the module selected by a front panel switch. When this turn on cycle is selected, the drive is turned off after 1.5 ms if the dee low threshold has not been reached and the pulse repeats at a 60 hz frequency.

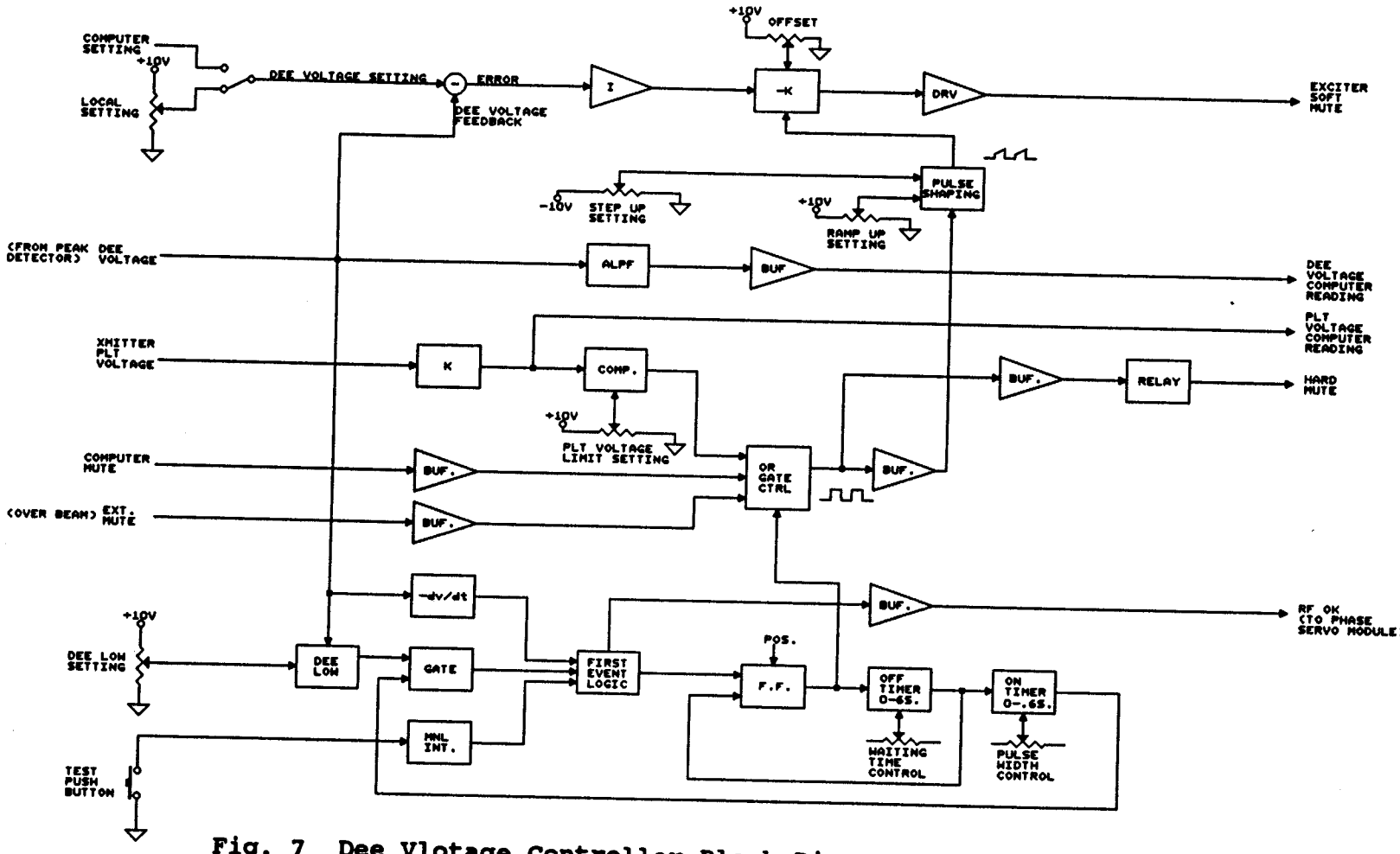

Fig. 7 Dee Vlotage Controller Block Diagram

Size	Document Number	RE
B		
Date:	July 31, 1990 Sheet	of

4. Target Control And Beam Monitor

The K100 cyclotron has two targets. The Main Target for full energy and high neutron yield is fixed in position at full radius and does not need control. The Popup Target is an air-cylinder actuated in or out device which inserts at the half energy point and allows the cyclotron to be tuned with external radiation reduced to about 1/50th of the full energy level. The computer can command the Popup Target to be inserted or retracted.

For monitoring beam current, two identical I/V converter channels are used, one for each target. The I/V converter generates a voltage proportional to the current (0 to 10V for 0 to 50ua) and also provides an interface to the computer.

5. Safety Interlocks

The K100 cyclotron control system utilizes both hardware and software interlocks. Software interlocks are relatively easy to implement and are intended to enforce needed personnel safety and equipment protection procedures when the cyclotron is in its normal operating mode. The software interlock system includes a code word secured bypass system, since many installation and initial check-out procedures are incompatible with some of the interlock requirements. Software interlocks have a time delay associated with the main loop timing of the control computer and, under worst conditions, their action can be delayed by several seconds. In places where either the time delay or the bypass feature of the software interlocks could be harmful, hardware interlocks are employed. These interlocks react quickly and reliably, and are the primary protection for equipment units such as the transmitter or the targets, where lasting damage could occur as a consequence of the time delay or the bypassing feature of the software interlocks. Hardware interlocks include a readout to inform the operator via the control computer of the interlocked condition. To protect against computer hangups, the control system includes a "Watchdog Timer" which will turn off the transmitter and the ion source power if the computer fails to reset the timer within a designated time.

The K100 cyclotron interlocks are summarized in Table IV.

References

1. Cancer Therapy Cyclotron For Harper Hospital, H.Blosser et al., NSCL Annual Report,167-169(1988).
2. Harper Cyclotron Technical Review, H.Blosser, Mar.5,1990, Unpublished.

Table IV. Control Interlocks

Cryostat & Magnet System:	
- Cryostat Vacuum High	
- Cryostat Temp. High	
- Cryostat Pres. High	
- Liquid He Level Low	
- Lead Drop High	
Ion Source System:	
- Source Water Flow Low	2 Channels
- Source Water Temp. High	2 Channels
- Source High Voltage Cable Out	
- Source Valve Open	
- Watchdog Timer	
rf System:	
- Xmitter Water Flow Low	
- Xmitter Water Pres. Low	
- Xmitter Water Temp. High	
- Xmitter Air Pres. Low	
- Xmitter Air Temp. High	
- PA Overload	
- Screen Overload	
- Resonator Water Flow Low	19 Channels
- Resonator Water Temp. High	19 Channels
- Cyclotron Vacuum High	
- Neutron Counts High	
- Watchdog Timer	
Target System:	
- Main Target Water Flow Low	
- Main Target Water Temp.High	
- Popup Target Water Flow Low	
- Popup Target Water Temp.High	

PRELIMINARY RF SYSTEM DESIGN FOR A 220 MEV PROTON THERAPY CYCLOTRON

J. Vincent, H. Blosser

Preliminary design studies are in progress at NSCL for a 220 MeV Proton synchrocyclotron to be used for proton therapy. This paper briefly discusses the rf parameters and the initial thoughts on achieving them.

The structure of the rf resonator being studied is a single conventional dee supported, tuned, and driven at 4 stem locations. If the magnet is azimuthally symmetric the needed frequency modulation range is from 88 to 65 Mhz; the needed range can be reduced if needed by adding azimuthally varying components ("hills and valleys") to the magnetic field; the difficulty of introducing this magnetic complexity will be evaluated versus the difficulty of achieving the full 88 to 65 Mhz range at a desired repetition rate of 1 kz. A dee voltage of 20 kilovolts is needed for 10-20 μs at the beginning of the cycle after which the voltage can sag to 10 kilovolts.

The fast sweep cycle requires the cavity to be electronically tuned rather than mechanically tuned (the technique used in the past on synchrocyclotrons). Two tuning methods were initially considered, namely:

1. Reactance Tube
2. Variable Biased Ferrites.

The variable biased ferrite technique has been chosen for further investigation because the reactance tube would require a great deal more power to operate.

Although ferrites are also quite lossy when used conventionally, it has been demonstrated elsewhere that the material Q increases dramatically when a DC bias field is applied.[1] It has further been demonstrated that when the modulating magnetic field is applied perpendicular to the rf magnetic field, a large excitation range is required, whereas when the modulating field is parallel to the rf magnetic field a much smaller range is required.[1] (As described in Ref. 1, this behavior is due to the perpendicular bias case causing the permeability to vary as B/H, whereas the parallel case varies the permeability as dB/dH.) However, if only one or the other of these techniques is used, the ferrite is very lossy for portions of the cycle and less so for other portions of the cycle depending on the modulation amplitude. The preferred method of modulation therefore uses "field rotation", i.e. two field components are used, one parallel to the rf magnetic field and the other perpendicular. Either both components or one of the components is varied in order to maintain high material Q while simultaneously varying the material permeability to obtain the desired frequency shift.

The method of modulation of the ferrite which looks most attractive in the geometry of the synchrocyclotron uses a static bias field component perpendicular to the rf field and a varying component parallel to the rf field. Depending on the material to be used, this will require the perpendicular component to be about 25% of the saturating field and the modulating field to vary by an amount which is also approximately 25% of the saturating value. This arrangement should simplify the electronic equipment, maintain high material Q, and give a reasonable modulating field range.

As mentioned earlier, the proposed cyclotron resonator structure is a single dee supported and driven at four stem locations. Two of the stems are currently envisioned to contain the ferrite tuners, one on the top and one on the bottom, symmetrically placed about

the center of the machine. The other two stems will contain the coupling loops to the driving system. One of these driving stems will contain the link to the driving tube connected in a self excited oscillator configuration, while the other stem will mirror the reactances of the driven stem to maintain system symmetry. It may also be possible to place the ferrite tuners in the cyclotron magnetic field in such a way as to use the cyclotron field to apply the necessary perpendicular static bias. This is the first arrangement that will be investigated in the following year to match the desired requirements.

We expect the rf portion of this project to proceed in the following manner:

1. Find and acquire as much information as possible on all the ferrite materials which may work for this application.

2. Begin analysis of the resonator structure to obtain the necessary impedance parameters to start a design process.

3. Design and build some simple structure to test samples of the likely ferrites for physical properties (as well as testing our understanding of these materials and their use).

4. Use all of the information gathered or derived from the above steps to attempt to design a rf structure that matches the desired requirements.

The above steps may lead to many conclusions. For example, it may not be possible to find a structure that fits in the magnet space currently being assumed by the accelerator physicists. Or it may not be possible to obtain the currently required frequency span or modulation rate. Should these problems occur, we will implement alternate approaches to the envisioned machine to match what can be done, for example, by enlarging the rf space, or by introducing azimuthal components into the magnetic field to cut done the frequency modulation range, etc.

In conclusion, an rf system for a 220 MeV synchrocyclotron is being studied, the overall goal of the project being to develop an accelerator optimized for use in cancer therapy. The rf group is starting the R&D phase of the rf system required and expects a detailed design for such an rf system to be developed in the coming year.

References

1. W.R. Smythe, "Reducing Ferrite Tuner Power Loss by Bias Field Rotation", IEEE Trans. on Nucl. Sci., Vol. NS-30,No. 4,2173(1983).

DIFFERENTIAL ALGEBRA BEAM OPTICS FOR PREDICTION OF S800 SPECTROGRAPH ERROR TERMS

A. Zeller, J. Nolen and M. Berz[a]

The optimizing ray tracing code MOTER[1] was used to calculate momentum and scattering angle resolutions for the S800 spectrograph.[2] Realistic measurement errors at the focal plane were used with error coefficients that represent coefficients of a polynomial relating focal plane coordinates of rays to their initial target coordinates. To get these coefficients relevant aberrations must be identified. These terms are found by taking the most significant terms from ray tracing, from looking at scatter plots of positions of sets of rays at the focal plane, and from trial and error. It should be noted that since X measurements and Y measurements at the focal plane translate to momentum and scattering angle, respectively, the possible number of aberration terms to fifth order is several thousand, but only about 50 of them are significant. The resolution is the residual left from subtracting this polynomial from the distribution of approximately 4000 rays at the focal plane. Finding these coefficients is a tedious process, since the effect of each coefficient can only be determined by running the code. With a running time of 30 minutes to over 4 hours, this is a very slow process.

The advent of differential algebra techniques[3] for beam optics calculations allows determination of significant aberrations up to any order. This allows the selection of error terms in a very short time. We have used the code COSY INFINITY to calculate aberrations for the S800 spectrograph as input for MOTER. At present, the code does not allow the use of gradients in dipole magnets and does not use fringe fields for multipoles. This means that the aberrations are not quite correct, but they offer an excellent starting point for choosing input for MOTER. The code is being changed to correctly include the effects of the dipole gradients and fringe fields. We will update our results when the modified code becomes available. As a test, MOTER calculations were done both with and without gradients in the dipoles. Shown in Table 1 are the error terms, listed as matrix elements in the standard TRANSPORT notation, derived from trial and error and used in MOTER calculations (called old terms in future discussions). Table 2 lists the significant matrix elements obtained from COSY INFINITY which are not listed in Table 1. Terms which are on both lists are marked with an "*". It should be noted that MOTER is run in a dispersion matched mode and that the measurement of X at the focal plane is a measure of momentum at the target. Similarly, Y measures scattering angle at the target. Thus terms like $x/\theta\delta$ and $x/\theta x$ are functionally indistinguishable in MOTER. These terms for x are listed in parentheses in Table 1. Similar terms for y are not shown for brevity.

MOTER calculations for momentum resolution and scattering angle resolution were made using assumed detector resolutions in x and y of 0.4mm and angular resolution $\Delta\theta=\Delta\phi=$ 0.3mr. Two extremes in solid angle and momentum acceptance were used (see contribution on S800 in this Report). The results are given in Table 3. The units of momentum and angular resolution are $\Delta p/p=$ 1 $X10^{-4}$ and $\Delta\theta=$ mr. Because of the way the code optimizes, an uncertainty of ±0.01 and ±0.02 in momentum and angular resolutions is implied. The 20% decrease in angular resolution with only the COSY terms is probably associated with not having fringe fields in the calculations, ie. some important terms are not

Table 1
Matrix elements used in MOTER obtained by trial and error.

x (momentum)	y (scattering angle)
$\theta\delta(\theta x)$ *	θy *
θ^2 *	$\theta\phi$ *
$\delta^2(x^2)$ *	$\phi\delta$ *
ϕ^2 *	$y\delta$ *
ϕy *	$y\delta$ *
y^2 *	$\theta^2 y$ *
θ^3 *	ϕ^3 *
$\theta^2\delta(\theta^2 x)$ *	$\theta^2\phi$ *
$\theta\delta^2(x^2\theta)$ *	$y\theta\delta$ *
$\theta\phi^2$ *	$\theta\phi\delta$ *
$\delta^3(x^3, x\delta^2)$ *	$\theta\phi^2$ *
$\phi^2\delta(\phi^2 x)$ *	$y^2\phi$ *
θ^4 *	$\phi\delta^2$ *
$\theta^2\phi^2$	$y\delta^2$ *
y^4	$\theta y\phi^2$ *
$\theta^3\delta(\theta^3 x)$ *	$\theta\phi^3$ *
$\phi^2 y^2$	$\theta^3\phi$ *
θ^5	$\phi^3\delta$ *
$\theta^3\phi^2$	$y\phi^2\delta$ *
$\theta\phi^4$	$\theta^2\phi\delta$ *
	$\theta y\phi^2\delta$
	ϕ^5
	$y^3\phi^2$
	$y^2\phi^3$

Table 2
Additional Matrix elements from COSY INFINITY

x	y
$\theta y\phi$	$x\theta^2\phi$
$x\theta^2\phi$	$\theta\phi\delta^2$
$\theta^2\delta^2$	
$\theta\delta^3$	
$\theta^3\delta^2$	

Table 3
S800 spectrograph resolutions

	No gradients in dipoles				Gradients			
	Ω=20,δ=.1		Ω=10,δ=2.5		Ω=20,δ=.1		Ω=10,δ=2.5	
	$\Delta p/p$	$\Delta\theta$	$\Delta p/p$	$\Delta\theta$	$\Delta p/p$	$\Delta\theta$	$\Delta p/p$	$\Delta\theta$
Old	0.49	0.53	0.46	0.50	0.49	0.51	0.46	0.51
Old+COSY	0.49	0.53	0.45	0.50	0.49	0.51	0.45	0.50
COSY only	0.50	0.62	0.45	0.63	0.50	0.61	0.45	0.64

Units are $\Delta p/p$=1 X10^{-4}, $\Delta\theta$= mr, Ω= msr, δ= ±%

indicated by the present version of COSY INFINITY.

It is apparent that COSY INFINITY will be very useful in spectrograph design for finding the required error terms in the shortest time, especially when the inhomogeneous sector magnet and multipole fringe field routines are added to the code. Taken together with MOTER this represents a big step forward in systematic spectrograph design and optimization.

---

a. LBL, University of California, Berkeley, CA

References

1. H.A. Thiessen, M. Klein and K. Boyer, LASL Report (1979) unpublished.
2. A.F. Zeller, L.H. Harwood and J.A. Nolen, MSU Annual Report 1981-82,88.
3. M. Berz, H.C. Hofmann and H. Wollnik, Nucl Instrum an Meth A258,402(1987; and M. Berz, Proc. II Conf on Codes used in Accelerator Physics, Los Alamos 1990 (in press).

SECOND ORDER ISOCHRONOUS ACHROMAT DESIGN WITH HOMOGENEOUS MAGNETS

D. Ioanoviciu and J.A. Nolen, Jr.

Second order isochronous achromats can be used in two major applications: 1) accelerator to target beam transport and 2) for time-of-flight mass measurements of exotic nuclei. Four or more consecutive cells are needed to transport a beam without adding transverse first order chromatic or second order geometric aberrations.[1] Generally, two sextupoles per cell are needed to completely achromatize the system at second order.[2] Flight time independence from the particle energy ("isochronism") is an essential feature in recoil fragment analysis.[3]

This note presents results for a very simple second-order isochronous achromat. The parameters of a system consisting of four identical homogeneous dipoles (all non-diagonal elements of the space-time matrix being less than 1.4×10^{-5}) are given below. No additional sextupoles are required.

To find the parameters of the second order isochronous achromat the conditions to be satisfied by the spatial matrix elements at the cell level, were incorporated in computer programs. Let A_i, A_{jk}, B_i, B_{jk} be the cell transfer matrix elements of the first and second row respectively. Assuming symmetric cells the first order conditions simplify:

$$A_x = B_a = A_y = B_b = 0 \qquad (1)$$

as well as those of second order:[4]

$$S_r = A_{xd} + B_{ad} + A_d(2B_{xx} + B_{xa}) = 0 \qquad (2)$$

for the radial plane,

$$S_{ax} = A_{dy} + B_{db} + A_d(A_{xy} + B_{xb}) = 0 \qquad (3)$$

for the axial direction. Here x is the distance of the particle from the beam axis in the bending plane, y is the distance perpendicular to that plane, a,b are the radial and the axial angle, and d the relative energy deviation of the particle, all related to the main path particle. (All notation is consistent with the program GIOS, with lengths in meters and angles in radians)

According to the simplecticity relations[5] the following time dependent coefficients of the whole achromat T_i, T_{jk} vanish:

$$T_x=T_a=T_{xx}=T_{xa}=T_{xd}=T_{aa}=T_{ad}=T_{yy}=T_{yb}=T_{bb}=0 \qquad (4)$$

The difference in flight time δt of some charged particle with respect to the reference particle (total flight time t_0) is related to the T coefficients through the relationship:

$$\delta t/t_o = T_x x + T_a a + T_d d + T_{xx}x^2 + T_{xa}xa + T_{xd}xd + T_{aa}a^2$$
$$+ T_{ad}ad + T_{dd}d^2 + T_{yy}y^2 + T_{yb}yb + T_{bb}b^2 \qquad (5)$$

Only T_d and T_{dd} are not obviously vanishing. Further calculations show that T_d is twice the cell time of flight element in d.

The cell geometry is completely defined by the following parameters (Fig. 1): ρ main path radius, ϕ deflection angle, ε beam entry and exit angle, L length of the drift space in front of and after the deflecting magnet, R entry and exit boundary curvature radius. The fringing field integrals I1 and I4 are detailed by the formulas:

$$I1 = \int_m^n [B(z)/B_o]\, dz\, dz - z_n^2/2 \qquad (6)$$

$$I4 = \int_m^n [B(z)/B_o]^2\, dz - z_n \qquad (7)$$

where B(z) is magnitude of the magnetic fringing field measured along the normal z to the field boundary, the point n being located inside the homogeneous field of intensity B_o while the point m is placed outside the fringing field (where negligible).

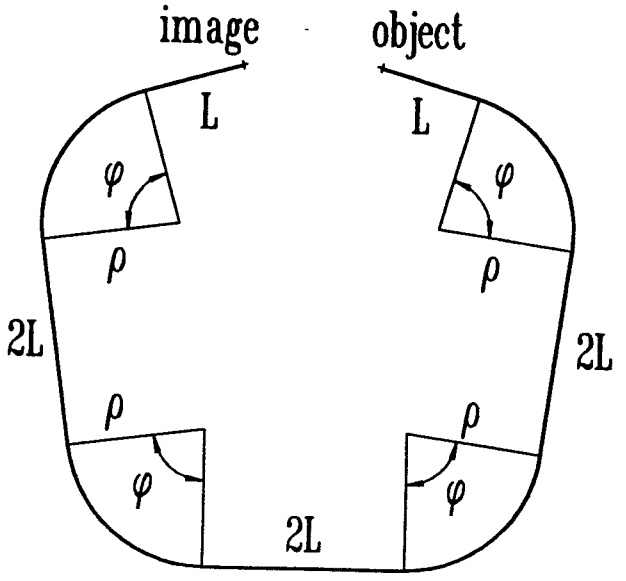

Fig. 1 Geometry of the second order isochronous achromat for the negligible fringing field case.

The search for isochronous achromat geometries contained the following steps: a) with I1 and I4 considered constants, a ϕ value is selected, and a pair of ε, L/ρ values is obtained that satisfies the first order condition (Eq. 1). b) next S_r is cancelled for some value of R (Eq. 2), while S_{ax} results from Eq. 3. Cycles are repeated to minimize S_{ax}.

Nineteen pairs of I1, I4 values taken from Ref.6, were used to calculate cell parameters assuming two magnet gap G to main path ρ ratios: 0.05 and 0.1 respectively. Throughout these calculations the condition (2) was always satisfied with an accuracy better than 5×10^{-6} while S_{ax} was around 10^{-5} in most cases. The resulting parameters are contained in the following ranges of values: ϕ between 82.554° and 86.053°, ε from 22.533° to 26.824° and L/ρ 0.7587 to 0.870.

For negligible fringing field integrals ϕ = 82.03346°, ε = 21.85647°, L = 0.74440 ρ, $\rho/R = 6\times10^{-6}$, are the parameters obtained for $S_r = 1.0\times10^{-7}$ and $S_{ax} = -4.8\times10^{-7}$. The system with these parameters run by the program GIOS[7] is a second order isochronous achromat as Table I shows (data from GIOS output). The nondiagonal matrix elements range from 5.3×10^{-12} to 1.4×10^{-5} for the second order transverse elements, and between 2.0×10^{-6} and 8.6×10^{-13} for the longitudinal (time dependent) elements up to second order. The third order transverse elements are reasonably low (values between 5.7×10^{-8} and 11.04×10^{-8}, not shown in the table). The time-of-flight performance deteriorates with increasing I1, I4 values. The fact may be attributed to the accumulation of the errors induced by these integrals at the cell level[8] by repeated matrix multiplication to obtain the final matrix elements. None of the geometries calculated here coincide with that of Ref. 3. As can be calculated from the data of that reference $T_{bb} = 0.1$. Without energizing the surface coils T_d is about 0.05 (calculated from the data of Fig. 5, Ref. 9).

The second order isochronous achromat geometry, for negligible integral values, offers in addition to the very good space-time focusing parameters a remarkable simplicity: absence of supplementary sextupoles or surface coils.

References

1. K.L. Brown, SLAC Pub. 2257(1979).
2. D.C. Carey, Nucl. Instrum. Methods 189,365(1981).
3. J.M. Wouters, D.J. Vieira, H. Wollnik, H.A. Enge, S. Kowalski and K.L. Brown, Nucl. Instrum. Methods Phys. Res. A240,77(1985).
4. D. Ioanoviciu and J.A. Nolen Jr, NSCL Annual Report 149(1988).
5. H. Wollnik and M. Berz, Nucl. Instrum. Methods Phys. Res. A238,127(1985).

6. Z.H. Hu, T. Matsuo and H. Matsuda, Int. J. Mass Spectrom. Ion Phys. 42,145(1982).

7. H. Wollnik, J. Heuser, T. Matsuo, E. Kasseckert, K. Becker, J. Brezina, C. Giesse, K. Lindemann, S. Meuser, J. Larson and J. Troetscher, Manual for GIOS, July 1988, II Phys. Inst. Universit. Giessen.

8. D. Ioanoviciu, Advan. Mass Spectrom. Vol.10, Ed. J.F.J. Todd, John Wiley Sons, 1986, page 857.

9. D.J. Vieira, Proceedings Int. Symp. on Heavy Ion Res. with Magn. Spectrogr., Eds. N. Anantaraman and B. Sherrill, NSCL, 1989, page 431.

Table I

Second Order Isochronous Achromat Transfer Matrix Elements

(x/x)=1.000, (x/a)=-1.216E-5, (x/d)=3.553E-11,

(a/x)=0.630E-5, (a/a)=1.000, (a/d)=-5.845E-6,

(T/x)=-1.001E-6, (T/a)=6.082E-12,(T/d)=2.048E-6,

(x/xx)=-3.253E-11, (x/xa)=-4.921E-6,

(x/xd)=2.717E-8, (x/aa)=1.539E-11,

(x/ad)=2.756E-6, (x/dd)=-2.519E-8,

(x/yy)=-1.555E-11, (x/yb)=1.425E-5,

(x/bb) = -6.793E-11,

(a/xx)=2.728E-6, (a/xa)=-3.237E-11,

(a/xd)=-1.042E-5, (a/aa)=2.461E-6,

(a/ad)=2.714E-8, (a/dd)=0.878E-5,

(a/yy)=5.950E-6, (a/yb)=-5.399E-12,

(a/bb)=0.806E-6,

(T/xx)=-6.332E-7, (T/xa)=5.211E-12,

(T/xd)=2.027E-6, (T/aa)=-7.766E-7,

(T/ad)=-4.311E-8, (T/dd)=-2.187E-6,

(T/yy)=-1.121E-6, (T/yb)=0.858E-12,

(T/bb)=-6.665E-7,

(y/y)=1.000, (y/b)=-0.884E-5,

(b/y)=2.892E-6, (b/b)=1.000,

(y/yx)=-1.006E-11, (y/ya)=1.425E-5,

(y/yd)=2.753E-11, (y/bx)=-1.611E-6,

(y/ba)=0.979E-11, (y/bd)=3.365E-6,

(b/yx)=1.190E-5, (b/ya)=-0.723E-10,

(b/yd)=-1.455E-5, (b/bx)=-0.998E-10,

(b/ba)=-1.425E-5, (b/bd)=1.108E-10.

TRIBOLOGY STUDIES: IMPLANTATION OF ^{7}Be AND ^{22}Na

M.L. Mallory, R.M. Ronningen, Y.X. Dardenne, Wm.C. McHarris, and H.J. Schock[a]

During the past several years we have developed an implantation technique potentially useful for tribology (wear studies).[1] The basis of the process is fragmentation of an ^{14}N beam on a C target, producing many low-Z species recoiling out of the target in the forward direction. These species can be implanted in a surface for wear studies. Of the radioactive nuclides produced, ^{7}Be has a reasonable half-life (53.3 d) and an easily identifiable γ ray (477.6 keV), making it useful for following surface wear. This technique has several important advantages over the older surface-layer-activation techniques: 1) It is independent of the Z of the material to be studied; hence, it is applicable to low-Z materials such as ceramics and plastics. 2) There is a factor of $\approx 10^{5}$ between the intensity of the primary (activating) beam and the radioactive species; thus, our technique causes far less "radiation" damage to the surfaces. On the other hand, the dose-depth profile of the activity in the surface is less constant (less a step function) than that for surface-layer activation, making it more difficult to deconvolute "average wear" over different locations in, say, an automobile engine.

Successful preliminary studies have been made on an Si_3N_4 ceramic disc. On the basis of such studies we have received funding from the State of Michigan, and the College of Engineering is now working toward developing a Wear-Studies Institute on campus.

This past year we have worked primarily on two facets of this project--to optimize the production of ^{7}Be and to seek other, complementary activities for implantation. In these runs we bombarded a stack of aluminium foils with a 40-MeV/A ^{14}N beam and with 18-, 30-, and 40-MeV ^{20}Ne beams. The recoils in the forward direction stopped in the stack of foils; the foils were later counted for γ-ray activity with a Ge detector. The activity as a function of foil number provides a dose-depth profile. (All the usual corrections were made for half-life, geometry, dead-time, absorption, etc.)

Figure 1 shows the dose-depth profile for ^{7}Be produced by 40-MeV/A ^{14}N and ^{20}Ne beams. The ^{14}N beam produces somewhat more ^{7}Be (roughly by a factor of 2), but the dose-depth profile is more compact and simpler in shape for the ^{20}Ne beam.

Figure 2 shows the ^{7}Be dose-depth profile for three different ^{20}Ne beam energies. The 30-MeV/A beam appears at first glance to yield the best profile, but further investigations need to be done on this.

The only other "practical" activity (moderate half-life, easily-identifiable γ rays) produced was 2.60-y ^{22}Na, produced by the ^{20}Ne beam. Figure 3 shows its dose-depth profiles for the three different beam energies. They are

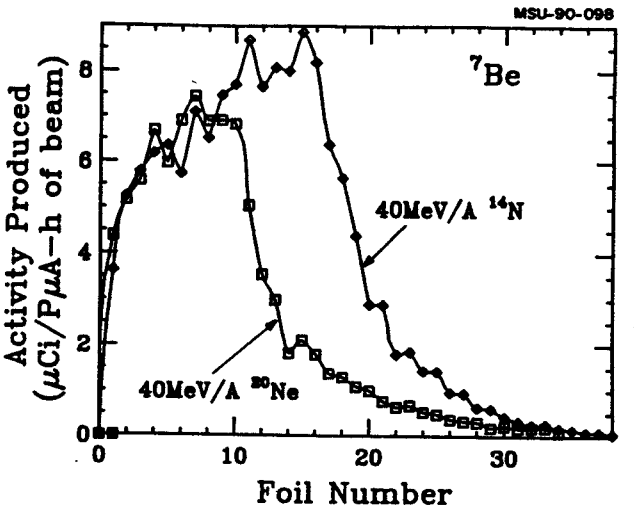

Fig. 1. ^{7}Be dose-depth profiles for ^{14}N and ^{20}Ne beams. Each Al foil was 28.5-mg/cm^2 thick.

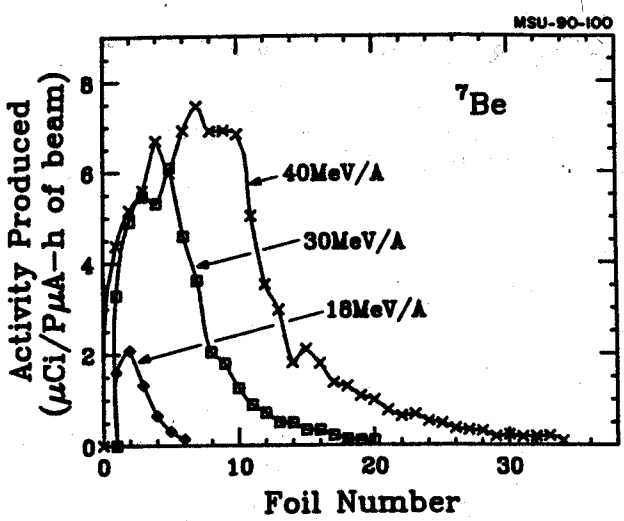

Fig. 2. ^{7}Be dose-depth profiles for three different ^{20}Ne beam energies. Each Al foil was 28.5-mg/cm^2 thick.

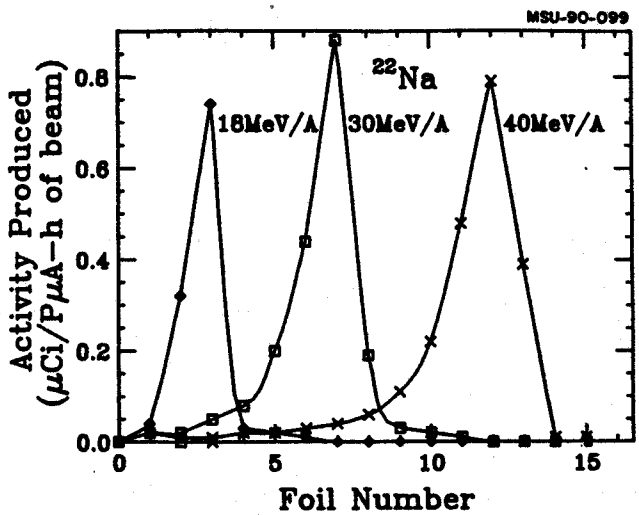

Fig. 3. ^{22}Na dose-depth profiles for three different ^{20}Ne beam energies. Each Al foil was 28.5-mg/cm^2 thick.

far simpler than the profiles for ^{7}Be. Also, it appears that the lowest beam energy (18-MeV/A) can provide the best profile (sharpest and closest to the surface). (^{22}Na is probably produced by simpler nuclear reactions than the complex fragmentation that produces ^{7}Be -- the profiles indicate some contribution from a compound-nucleus type of reaction, but this is undoubtedly an oversimplification -- determining the formation mechanism would be a major research project in itself.)

^{22}Na now appears to be at least as good as ^{7}Be for implantation, for the following reasons: 1) Its dose-depth profile is sharper, most likely allowing for studies of "average wear" as done by surface-layer activation. 2) Its production cross-section is considerably higher, allowing for shorter, cheaper bombardments (studies are planned for assessing this more quantitatively). 3) Its production requires a lower-energy beam, thus allowing for a less expensive cyclotron or other accelerator. Its most obvious drawback is that the primary beam does not get stopped so easily. (The dE/dx values for ^{7}Be and ^{14}N, for example, are different enough to allow one to stop the primary beam easily, allowing only the ^{7}Be to strike the implantation surface -- the difference is not so great and of the wrong sign for ^{20}Ne and ^{22}Na.) An added bending magnet between the production target and implantation position might filter out the primary beam fairly efficiently, but high transmission efficiency would be needed.

In summary, although considerable developmental work remains to be done, ^{22}Na, ^{7}Be, and/or the two in combination are likely to be powerful tools for tribology studies. With the addition of ^{22}Na, the techniques combine most of the advantages of ^{7}Be implantation and surface-layer activation.

---

a. College of Engineering

References

1. M.L. Mallory, R.M. Ronningen, Wm.C. McHarris, B. Sherrill, Y.X. Dardenne and H.J. Schock, Nucl. Instr. & Meth. B40/41(1989)579.